Bioactive Materials 40 (2024) 1–18

Contents lists available at ScienceDirect

Bioactive Materials

journal homepage: www.keaipublishing.com/en/journals/bioactive-materials

Mitochondria-engine with self-regulation to restore degenerated intervertebral disc cells via bioenergetic robust hydrogel design

Juehan Wang [1], Yulin Jiang [1], Ce Zhu, Zheng Liu, Lin Qi, Hong Ding, Jing Wang, Yong Huang, Yubao Li, Yueming Song, Ganjun Feng [***], Li Zhang [**], Limin Liu [*]

Analytical & Testing Center, Department of Orthopedic Surgery and Orthopedic Research Institute, West China Hospital, Sichuan University, Chengdu, 610065, China

ARTICLE INFO

Keywords:
Mitochondrial dysfunction
Intervertebral disc degeneration
L-arginine
ROS scavenging
Polyurethan scaffold

ABSTRACT

Previous studies have confirmed that intervertebral disc degeneration (IDD) is closely associated with inflammation-induced reactive oxygen species (ROS) and resultant cell mitochondrial membrane potential (MMP) decline. Clearance of ROS in an inflammatory environment is essential for breaking the vicious cycle of MMP decline. Additionally, re-energizing the mitochondria damaged in the inflammatory milieu to restore their function, is equally important. Herein, we proposed an interesting concept of mitochondrion-engine equipped with coolant, which enables first to "cool-down" the inflammatory environment, next to restore the MMP, finally to allow cells to regain normal energy metabolism through materials design. As such, we developed a multi-functional composite composed of a reactive oxygen species (ROS)-responsive sodium alginate/gelatin hydrogel infused into a rigid 3D-printed thermoplastic polyurethane (TPU) scaffold. The TPU scaffold was coated with conductive polypyrrole (PPy) to electrophoretically deposit L-arginine, which could upregulate the Mammalian target of rapamycin (*mTOR*) pathway, thus increasing MMP and energy metabolism to stimulate extracellular matrix synthesis for IVD repair. While the ROS-responsive hydrogel acting as the "mito-engine coolant" could scavenge the excessive ROS to create a favorable environment for IVD cells recovery. Demonstrated by *in vitro* and *in vivo* evaluations, the mito-engine system markedly promoted the proliferation and collagen synthesis of nucleus pulposus cells while enhancing the mitochondrial respiration and MMP under oxidative stress. Radiological and histological assessments *in vivo* revealed the efficacy of this system in IVD repair. This unique bio-inspired design integrated biomaterial science with mitochondrial biology, presents a promising paradigm for IDD treatment.

1. Introduction

Intervertebral disc degeneration (IDD) is a significant clinical challenge, contributing extensively to back pain and disability in the aging population. This degenerative process is characterized by the deterioration of disc structure and function, which is influenced by mechanical load, genetic predisposition, and biochemical changes within the disc cells. Critically, mitochondrial dysfunction is increasingly recognized as a central player in IDD.

Functioning as the "energy-generating engine", mitochondria enable efficient energy production in eukaryotes, with the mitochondrial respiratory chain (MRC) as the central process which features delicate orchestration between electron transport chains (ETC) and adenosine triphosphate (ATP) synthesis on the inner mitochondrial membrane (IMM). In the context of IDD, mitochondrial dysfunction is marked by decreased production of ATP and an increase in reactive oxygen species (ROS) [1,2]. This mitochondrial impairment contributes to cellular energy deficits and oxidative stress, which exacerbate matrix degradation and inhibit the reparative capabilities of disc cells. Highlighting the mitochondria's role provides a foundational understanding of their dual involvement in both the degeneration and potential regeneration of the intervertebral disc (IVD) [3,4].

Peer review under responsibility of KeAi Communications Co., Ltd.
* Corresponding author.
** Corresponding author.
*** Corresponding author.
E-mail addresses: gjfenghx@163.com (G. Feng), zhangli9111@126.com (L. Zhang), liulimin_spine@163.com (L. Liu).
[1] The two authors contributed equally to the work.

https://doi.org/10.1016/j.bioactmat.2024.05.044
Received 19 December 2023; Received in revised form 27 May 2024; Accepted 28 May 2024

Recent bioengineering approaches to treat IDD have largely concentrated on direct ROS scavenging, aiming to reduce oxidative stress within the disc environment [5–8]. Although effective in mitigating immediate oxidative damage, these approaches do not address the resultant organelle dysfunction, particularly of mitochondria, which is crucial for cellular energy supply and overall cell health. This oversight means that merely clearing ROS without restoring mitochondrial function may not lead to satisfactory repair outcomes, as the cells continue to suffer from impaired energy metabolism and reduced regenerative capacity.

Previous literature highlighted the growing importance of arginine, a conditionally essential amino acid, in the inflammatory environment [9]. Also, the metabolic byproducts of L-arginine participate further in the tricarboxylic acid cycle [10]. Therefore, L-arginine is generally classified as the bioenergetic amino acid based on its nature to promote energy metabolism and protein synthesis [11], and has already exerted favorable therapeutic efficacy in the applications of cardiac and wound healing [12,13]. Therefore, it may be a unique perspective and approach of to treat IDD through elevating the MMP and restoring the energy metabolism of impaired IVD cells by means of incorporating L-arginine.

Our research introduces a novel "mito-engine" system, a bioenergetic hybrid hydrogel designed to address the mitochondrial dysfunction observed in degenerated IVD cells. This bioenergetic biomaterial system was constructed by a functionalized 3D-printed thermoplastic urethane (TPU) scaffold interpenetrated with 4-Aminophenylboronicacidpinacolester (AB) sodium alginate/gelatin (SA/GEL) composite hydrogel (R-AG). Of which, the TPU scaffold was firstly functionalized by polypyrrole (PPy) to possess conductivity, and then coated by L-arginine through electrophoretic deposition (EPD). This enabled the scaffold to release L-arginine into IDD environment. The released L-arginine could activate the mTOR pathway and elevate the mitochondrial membrane potential. The ROS-responsive composite hydrogel incorporated in the system could combat the escalated ROS level as well as the inflammation commonly found in degenerated intervertebral disc environment, thus creating suitable conditions for IDD repair. The hybrid system integrated with a rigid TPU scaffold and a soft hydrogel highly simulated the rat's natural IVD structure, not only meeting the stringent mechanical requirements but also providing optimal support for disc rejuvenation. We conceptually termed this hybrid material system as "mito-engine" and its compositions and working mechanism were described in Fig. 1.

2. Materials and methods

2.1. Preparation of raw materials

Thermoplastic polyurethane (TPU) was obtained from Shanghai Yuanzhu intelligent Technology Co., LTD. Sodium alginate (SA), gelatin, 4-Aminophenylboronicacidpinacolester (AB) and L-arginine were purchased from Shanghai Aladdin Biochemical Technology Co., LTD. Sodium periodate and borax were purchased from Chengdu Jinshan Chemical Reagent Co., LTD. Hydrogen peroxide (H_2O_2) was obtained from Chengdu Kelong Co., LTD. Titanium sulfate ($Ti(SO_4)_2$) was provided by Shanghai Maclin Biochemical Technology Co., LTD.

2.2. Preparation of TPU-aa scaffold

The model of TPU scaffold was exported into STL format for 3D

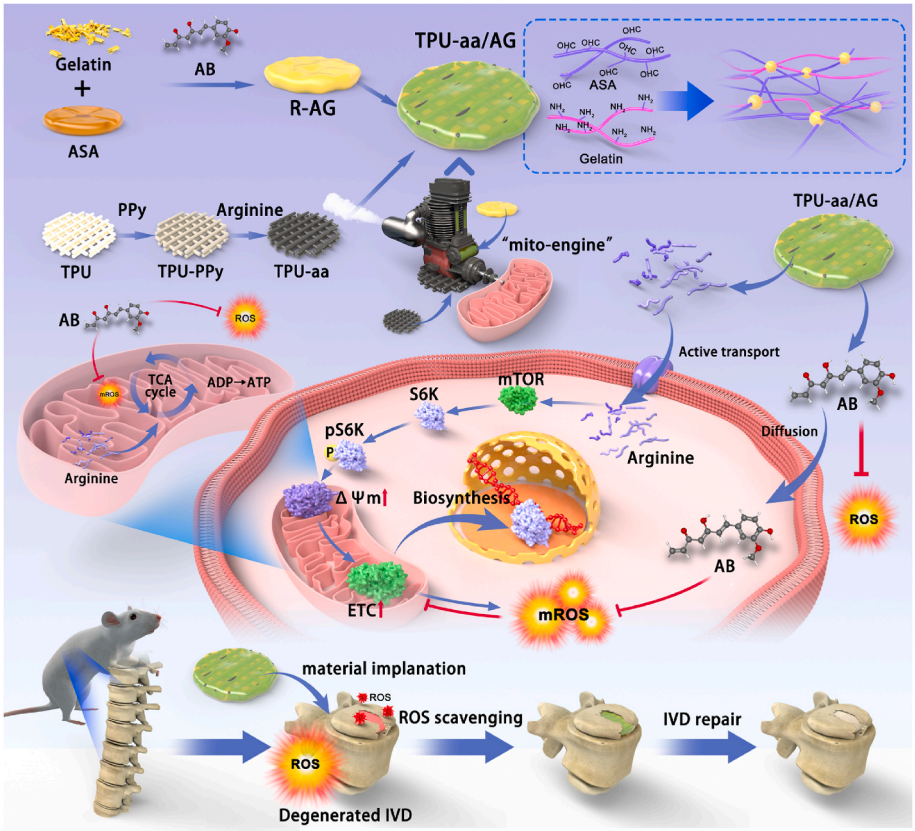

Fig. 1. Schematic diagram illustrating the synthesis of "Mito-Engine" and its mechanism to promote intervertebral disc regeneration via enhancing the mitochondrial membrane potential. PPy: polypyrrole. AB: 4-Aminophenylboronicacidpinacolester. ETC: electron transport chains. TPU: thermoplastic urethane. TPU-PPy: TPU scaffold functionalized by PPy. TPU-aa: TPU-PPy scaffold coated by L-arginine. ASA: oxidized alginate. ROS: reactive oxygen species. R-AG: ROS-responsive alginate/gelatin (SA/GEL) composite hydrogel. TPU-aa/AG: TPU-aa scaffold interpenetrated with R-AG hydrogel. IVD: intervertebral disc. ETC: electron transport chains. mTOR: mammalian target of rapamycin. S6K: ribosomal S6 kinase. ΔΨm: mitochondrial membrane potential. TCA: tricarboxylic acid.

printing using a selective laser sintering (SLS) equipment (EP- 3650, China). The printing speed was 200 m/s and the part bed temperature was set at 100 °C. The printed TPU scaffolds was soaked in ethanol for 1 h, and then removed and dried. The scaffolds were immersed in a freshly prepared reaction mixture containing $FeCl_3$ and pyrrole at a molar ratio of 2.33:1 in deionized (DI) water, then the reaction mixture was stirred at 37 °C for 24 h and then removed and washed thoroughly with DI water. After that, the scaffolds were freeze-dried to obtain PPy coated TPU scaffolds (TPU-PPy). Carbon rod (the anode) and TPU-PPy (the cathode) were immersed in 300 mL 1 % (w/w) L-arginine solution in the electrochemical cell. Then, EPD was carried out for 60 min under a DC voltage of 25 V to obtain the amino acid coated sample, which was dried and named as TPU-aa.

2.3. Synthesis of ROS responsive aldehydrated SA/gelatin (R-AG) hydrogel

Sodium alginate (SA) was oxidized using the method as described previously [14]. Briefly, 2 g SA powder was dissolved into 10 mL ethanol, followed by the addition of 10.8 g sodium periodate as the oxidizing reagent at room temperature. The mixture was further stirred for 6 h at room temperature in the dark and centrifuged to collect the precipitate. After repeated washing with ethanol and then lyophilized, the oxidized alginate was obtained and named as ASA.

Subsequently, SA (4 wt%) and borax (2 wt%) were dissolved homogeneously in DI water at 37 °C with stirring, followed by the addition of gelatin solution (8 wt%) and 4-Aminophenylboronicacidpinacolester (AB) (0.5 wt%). The mixture solution was left to set at 37 °C for 6 h and then at room temperature for 24 h to obtain the final composite hydrogel, which was named as R-AG.

2.4. Preparation of TPU-aa/AG hybrid hydrogel

The 3D-printed TPU-aa was infused with the precursor solution of the R-AG hydrogel under negative pressure to ensure the thorough infiltration into the interior of the scaffold, then repeated five times to get the resulting hybrid hydrogel that was named as TPU-aa/AG.

2.5. Materials characterization

The morphologies and elemental compositions of samples were characterized by scanning electron microscopy (SEM, JSM-7500F, JEOL, Japan), stereomicroscopy (Nikon SMZ800, Japan), and energy-dispersive spectrometry (EDS, JSM-7500F, JEOL, Japan). Fourier transform infrared spectrometer (FTIR, Nicolet 6700, Thermo Scientific, USA) and X-ray photoelectron spectroscopy (XPS, XSAM800, Kratos, England) were used to analyze the interactions between chemical compositions in samples. The surface wettability of TPU, TPU-PPy and TPU-aa was analyzed using a contact angle measurement instrument (JY-82A, Chengde Dingsheng Co. LTD, China). The electrical conductivity of TPU-PPy was measured by the four-point probe method (RTS-9, Guangzhou 4 probes Co. Ltd., China). L-arginine concentrations were measured using an L-Arginine Assay Kit (Abcam, ab241028) according to the manufacturer's instructions.

The water content (W_C) and swelling ratio (W_S) of the hydrogels were measured by the gravimetric method. The cylindrical hydrogels (Φ = 7.5mm × 16 mm) were lyophilized to constant weight and weighed. Five hydrogels were tested to get the mean value for analysis. The W_C was calculated from Equation (1):

$$W_C\ \% = \frac{W0 - W1}{W0} \times 100\% \quad (1)$$

where W0 and W1 are the weight of the hydrogel before and after drying, respectively.

Hydrogels were soaked in DI water at 37 °C for 24 h, then taken out and weighed at different time intervals (1 d, 3 d, 5 d, 7 d, and 10 d) after removing the excess water on the surface. The swelling ratio (W_S) was calculated according to Equation (2):

$$W_S\ \% = \frac{W2 - W1}{W1} \times 100\% \quad (2)$$

where W1 is the initial weight of the hydrogel, and W2 is the swollen weight of the hydrogel.

The cylindrical specimens (Φ = 7.5mm × 16 mm) of the pure hydrogel, TPU scaffold and hybrid hydrogel were tested using a universal mechanical testing machine (INSTRON 5967, America). All samples were compressed at a speed of 2 mm/min and stopped until a 40 % compression ratio. The loading/unloading behaviors of the hydrogels were investigated through three loading/unloading cycles (compressing to 40 % or 80 % strain and unloading to 0 % strain) using a universal mechanical testing machine (INSTRON 5967, America). For each sample, five parallel specimens were tested to get the mean value for analysis. The corresponding elastic modulus was calculated from the region of linear change in the stress-strain curve. Five parallel specimens for each group were tested for getting the average.

2.6. Finite element simulation

To obtain the material constitution for the simulations, standard compressive tests of materials were carried out for comparison to the simulation, and the simulation results displayed a similar pattern of significant qualitative and quantitative agreement with the experiment. Quasistatic uniaxial compression simulations were performed in the *z*-axial direction via ABAQUS software. Details regarding the parameter settings for the finite element analysis can be found in the Supplementary Information.

2.7. ROS-scavenging ability evaluation

Cylindrical R-AG hydrogel (Φ = 14mm × 2 mm) was immersed in 8 mL DI water and the H_2O_2 solution (100 μM), respectively, and oscillated in a shaking table at 37 °C. After 1 h and 4 h, 2 mL of the supernatant was taken out, followed by adding 2 mL liquid back correspondingly. ICP-OES (AXIS Ultra DLD, Kratos, UK) was used to test the concentration of B element in the solution.

The H_2O_2 solution (100 μM) was incubated with the R-AG hydrogel (200 mg) overnight at 37 °C. Then 1 mL of the above solution and 2 mL $Ti(SO_4)_2$ (0.03 mM) were mixed to obtain homogeneous solution. The color change and absorbance spectra of the mixture solution were recorded and measured to determine the H_2O_2 scavenging ability of R-AG.

2.8. Primary nucleus pulposus (NP) cells isolation

The primary NP cells were isolated from lumbar discs of Sprague–Dawley rats (6–8 weeks old, 200–250 g). The lumbar segments of the spine were extracted integrally under sterile conditions and lumbar discs were collected. Gelatinous NP tissues were separated using a sized 11 surgical blade with a dissecting microscope and digested in 0.25 % trypsin and 0.1 % type II collagenase (Invitrogen, Carlsbad, CA, USA) for 4 h at 37 °C. The digestion medium was similarly washed and filtered after centrifugation at 1000 rpm for 5 min, and the sediment was resuspended in Ham's F12 medium (Thermo Fisher Scientific) supplemented with 10 % fetal bovine serum (FBS, Gibco) and 1 % antibiotics (penicillin/streptomycin) in an incubator containing 5 % CO_2 at 37 °C. The culture medium was replaced every two days. The primary NP cells were immunofluorescently stained for collagen type II (Col 2), aggrecan, keratin 19 (Krt19), and collagen type I (Col 1) to verify their purity and confirm the absence of annulus fibrosus (AF) cell contamination (Fig. S14). Cells from passages 1 to 3 were used for the following

experiments.

2.9. Cell biocompatibility

The live/dead staining assay was conducted to assess the effects of TPU, TPU-aa, R-AG, and TPU-aa/AG on the proliferation and biotoxicity of NP cells. NP cells (1.0×10^5/mL) were seeded in the lower chamber of a 24-well transwell plate (Corning, USA), while TPU, TPU-aa, R-AG, and TPU-aa/AG were separately cultured in the upper chamber. Cells were incubated with 500 μL Calcein AM/PI working solution (Beyotime, China) for 30 min on day 1, 3, and 5, followed by observation under a fluorescence microscope (ZEISS, Germany). Furthermore, a CCK-8 detection kit (Dojindo, Japan) was employed to quantify cell proliferation post-treatment with TPU, TPU-aa, R-AG, and TPU-aa/AG. In brief, NP cells (0.8×10^5/mL) were cultured in 24-well transwell plates, with TPU, TPU-aa, R-AG, and TPU-aa/AG in the upper chamber. On days 1, 3, and 5, the lower chamber was supplemented with 10 μL of the CCK-8 solution. Following 1 h incubation at 37 °C, the absorbance value was determined at 450 nm using a FlexStation 3 microplate reader (Molecular Devices, Japan). We seeded 1×10^6 NP cells onto each material group and cultured them in 24-well plates for 3 days. Subsequently, each material group was incubated with Calcein AM/PI working solution for 30 min. The adhesion and proliferation of cells on different groups were then examined under a confocal laser scanning microscopy (CLSM).

2.10. Sequencing

Total RNAs were used for RNA sequencing library preparation using KCTM Stranded mRNA Library Prep Kit for Illumina® (Catalog NO. DR08402, Wuhan Seqhealth Co., Ltd. China) following the manufacturer's instruction. PCR products corresponding to 200–500 bps were enriched, quantified and finally sequenced on DNBSEQ-T7 sequencer (MGI Tech Co., Ltd. China) with PE150 model.

2.11. Seahorse metabolic analysis

NP cells (1×10^5 cells/well) were seeded onto XF-24 cell culture plates (Agilent Technologies) and incubated overnight. To establish the oxidative stress model, 100 μM H_2O_2 was added, followed by supplementation with different experimental materials for each group. After a 12 h treatment period, cellular oxygen consumption rates were measured using an XF-24 flux analyzer (Agilent Technologies). NP cells were first exposed to 2.0 μM oligomycin to assess ATP production in each group, then 1 μM carbonyl cyanide-*p*-trifluoromethoxyphenylhydrazone (FCCP) was introduced to the supernatant to evaluate the enhanced rate of mitochondrial oxygen consumption, which was designated as the maximum oxygen consumption capacity of mitochondria. Lastly, 0.5 μM antimycin A and 0.5 μM rotenone were added to inhibit the mitochondrial respiratory chain (MRC) and entirely suppress mitochondrial oxygen consumption.

2.12. Evaluation of intracellular ROS, mitochondrial membrane potential, and mitochondrial morphology

According to the previous literature [15], NP cells were seeded in a 6-well plate, and 100 μM H_2O_2 was added to establish an oxidative stress model. The cells were divided into six groups, that is, Control, Blank, TPU, TPU-aa, R-AG and TPU-aa/AG. For ROS detection, cells were treated with DCFH-DA (10 μM) (Beyotime, China) for 20 min, washed 3 times, and observed under a microscope. To measure mitochondrial membrane potential, cells were stained with the JC-1 Membrane Potential Detection Kit (Beyotime, China) for 30 min and then observed under a microscope and then samples were finally analyzed using a flow cytometry and Flowjo 7.6.1 software. For mitochondrial morphology observation, cells were scraped with a cell scraper, centrifuged at 3000 rpm for 5 min to discard the supernatant, then glutaraldehyde fixative solution pre-cooled to 4 °C was slowly added. After dehydration, samples were sliced in the LEICA EM UC7 ultrathin microtome to obtain 70–90 nm slices. The slices were stained with lead citrate solution and uranyl acetate 50 % ethanol saturated solution for 5–10 min and air-dried before observation in a biological TEM (Hitachi H-7650).

2.13. Imaging validation

At eight weeks post-operation, all rats were imaged using an American Faxitron X-ray system (32 kV voltage, 10-s exposure time) and a high-resolution microcomputed tomography (micro-CT) imaging system (SkyScan 1172, BrukerBioSpin, Belgium). Based on the micro-CT scan and reconstruction results, the intervertebral disc height (IDH) and the relative osteophyte volume were evaluated. Magnetic resonance imaging (MRI) of intervertebral discs were detected to monitor the degeneration or regeneration of intervertebral discs. The detailed MRI Pfirrmann grading system was shown in the Supplementary Table S3.

2.14. Rat IDD model and the implantation of materials

This study was conducted in accordance with the guidelines approved by the Institutional Animal Care and Use Committee of West China Hospital, Sichuan University (approval number: 20220718002). For *in vivo* experimentation, 8-week-old Sprague Dawley male rats (282.90 ± 15.87 g) were randomly selected from the Animal Center of Sichuan University. The rats were then anesthetized using isoflurane inhalation. The surgical procedure for inducing intervertebral disc degeneration (IDD) in rat models followed previously established methods. In summary, a 21-gauge needle was percutaneously inserted into the center of the nucleus pulposus (NP) through the annulus fibrosus at the Co5-6 or Co6-7 level. The needle was then rotated 180° and held in place for 5 s, with locking forceps clamped at a distance of 5 mm from the needle to ensure consistent depth. The sham operation group ($n = 5$) underwent only anesthesia and skin incision, with no intervertebral disc damage inflicted. The IDD rats ($n = 25$) were divided into five groups with the IDD group ($n = 5$) as the negative control, and TPU ($n = 5$), TPU-aa ($n = 5$), R-AG ($n = 5$), and TPU-aa/AG ($n = 5$) were respectively implanted or injected into the intervertebral disc at the second weeks after surgery (Fig. S13). All animals completed the study as planned, and there were no deaths or removals from the study. The histological grading system (Supplementary Table S2) was assessed using established criteria: scores of 5 indicated normal discs, 6−11 indicated moderate degeneration, and 12−15 indicated severe degeneration.

2.15. qRT-PCR

qRT-PCR assays were conducted according to the methods outlined in reference [16]. Briefly, the total RNA from nucleus pulposus (NP) cells was isolated using the RNeasy Mini Kit (Qiagen, USA), following the manufacturer's protocols. RNA concentration was determined using a NanoDrop ND-1000 Spectrophotometer (NanoDrop Technologies, USA), and then reversely transcribed with PrimeScript™ RT Master Mix (Takara, China) as per the manufacturer's instructions. Polymerase chain reaction (PCR) amplification conditions were set as follows: 35 cycles at 95 °C for 4 min, 95 °C for 20 s, 60 °C for 30 s, and 72 °C for 30 s; followed by an additional extension at 72 °C for 10 min. Primer sequences were provided in Supplementary Table S1. Fold changes of targeted mRNAs were calculated using the $2^{-\Delta\Delta Ct}$ method, with β-actin serving as the reference gene.

2.16. Western blots

Western blot analysis was performed according to the previous reference [16]. Briefly, samples were treated with 100 μL of RIPA lysis buffer for 15 min to extract total protein. Standard protocols were

followed for Western blotting. Proteins were initially separated using a 10 % sodium dodecyl sulfate-polyacrylamide gel electrophoresis (SDS-PAGE), and the resolved protein bands were subsequently transferred onto polyvinylidene fluoride membranes (Amersham, UK). The membranes were blocked with 5 % skim milk for 2 h and incubated overnight at 4 °C with primary antibodies against phospho-mTOR-S2448, total mTOR, phospho-p70 S6K, and total p70 S6K. Protein bands were visualized using the ChemiDoc™ XRS + system (Bio-Rad Laboratories, USA).

2.17. Immunohistochemistry

Intervertebral disc (IVD) paraffin sections underwent antigen retrieval by incubation in citrate buffer (pH 6.0) (Servicebio, G1202) and microwaving on high heat for 6–8 min. To prevent nonspecific protein binding, sections were blocked with 5 % bovine serum albumin (BSA) at room temperature for 30 min. Subsequently, sections were incubated overnight at 4 °C with primary antibodies anti-Col 2 and *anti*-mTOR. Following this, sections were incubated with appropriate secondary antibodies for 1 h at ambient temperature. The DAB detection system (abs996, Absin) was employed to visualize positive staining. Finally, sections were dehydrated, sealed, and digitally scanned using a slide scanner.

2.18. Immunofluorescence

Immunofluorescence staining was conducted as previously described to assess Col2 expression in the NP cells. After 24 h, the cells were washed twice with phosphate-buffered saline (PBS) and subsequently fixed using 4 % paraformaldehyde for 10 min. The fixed cells underwent treatment with 0.1 % Triton X-100 for 15 min, followed by incubation with anti-Col2 polyclonal antibody (Servicebio, China) at 4 °C overnight. On the subsequent day, fluorescein isothiocyanate (FITC)-labeled and Cy3-labeled immunoglobulin (Ig)G (Servicebio, China) were employed to label Col2 and mTOR antibodies, respectively, at room temperature for 1 h. The cytoskeleton was stained using Cy3-labeled phalloidin (Servicebio, China), while the cell nuclei were stained with 4′,6-diamidino-2-phenylindole (DAPI) (Servicebio, China). Fluorescent images were acquired using a CLSM (ZEISS, Germany) and quantified with ImageJ software.

2.19. Histological analysis

At the 8th week post-operation, all rats were euthanized. IVD samples were collected, fixed in 4 % paraformaldehyde, decalcified, and then embedded for sectioning. Histopathological characteristics were assessed using hematoxylin and eosin (H&E) staining, Masson staining, and Safranin O-fast green staining. Histological results for assessing the disc degeneration were qualified by histological scores based on the previous method [17].

2.20. Statistical analysis

Statistical analysis was conducted utilizing SPSS 23.0 (IBM Corp., Armonk, NY, USA) and GraphPad Prism 9 (GraphPad Software, USA). The collected data were tested for normality by Shapiro-Wilk normality test. The independent samples *t*-test assessed the statistical difference between two groups, while one-way analysis of variance (ANOVA) was employed for multiple data group comparison. Data are expressed as mean ± standard deviation. A p-value <0.05 was statistically significant.

3. Results and discussion

3.1. Construction of "mito-engine" equipped with coolant

TPU is a durably biocompatible and robust elastomer that draws considerable interest in the applications of tissue implants [18,19]. Refer to our previous work [20], the simple cubic model was selected as a 3D model. While PPy as a rarely electroconductive polymer, has also been widely applied in biomedical field due to its good biocompatibility and easy polymerization on the surfaces of devices [21,22]. In this study, PPy was coated on the internal and external surfaces of the TPU scaffold through *in-situ* polymerization, enabling the electrophoretic deposition of electrically charged L-arginine on it [23]. SEM images (Fig. 2Aa) show that TPU, TPU-PPy, and TPU-aa scaffolds all exhibit a uniform porous structure with a pore size of 200 μm. Fig. S1 shows that the PPy submicron particles with electrical conductivity of 23.60×10^{-4} S/m could be successfully synthesized. And Fig. S2 displays that the *in-situ* polymerization of PPy with the following deposition of L-arginine made the TPU scaffold change from white to black. Apparently, the surfaces of TPU-PPy and TPU-aa scaffolds are in granular and plate-like forms after the modification of PPy and L-arginine, respectively, favorable to cell attachment and growth. And the EDS mapping showed that the C, N, and O was uniformly distributed on the platelet-like arginine on the surface of TPU-aa scaffold (Fig. 2Ab). From XPS results as shown in Fig. 2Ac, N1 peaks appeared in XPS surveys of TPU-PPy and TPU-aa in comparison to TPU. The new characteristic peak of C1s deconvolution at 288.1cm-1 corresponded to –COO appearing at TPU-aa in contrast with TPU-PPy, verifying the successful deposition of L-arginine on the PPy functionalized TPU scaffold. The TPU and TPU-PPy have a rough surface and the contact angle of TPU-PPy is$70.62° \pm 1.24°$ (Fig. S3), but after EPD, the water droplet dropped on TPU-aa rapidly spread out within 0.1 s to show a contact angle close to 0°, implying the successful deposition of hydrophilic L-arginine (**Figure Ad**). The release profile of L-arginine from the TPU-aa scaffold was displayed in Fig. 2Ae. L-arginine was released slowly in the first 3 days and then reached a balance, and the release amount reached the effective concentration according to numerous reports [24–26].

Sodium alginate (SA) as a naturally biocompatible polysaccharide, has been applied in the repair of degenerative IVD [27]. The application of hydrogels based on the imine linkage of oxidized SA and gelatin in biomedicine could be further broadened [28]. The formation and dissociation of the boronic ester derivatives exhibited an enhanced ROS-sensitivity [29]. The amido group on the 4-Aminophenylboronicacidpinacolester and the carboxyl group on the sodium alginate undergo amidation reaction (Fig. S4). We first carried out the experiment of oxidized SA followed established protocols in the published work [14,30], the FTIR spectra of oxidized SA showed that the aldehyde group was formed by the oxidation of SA (Fig. S5). Next we synthesized the ROS-responsive hydrogel (R-AG) through Schiff's base reaction between the oxidized SA and the gelatin, with the concurrent introduction of 4-Aminophenylboronicacidpinacolester, accompanied by an obvious color change from colorless to pink (Fig. S6). SEM images (Fig. S7) shows that R-AG hydrogel has a typical porous network structure with uniform pore size, which is beneficial for the diffusion of small molecule drugs and nutrients. And the R-AG hydrogel also behaved an increasing swelling ratio over time, until reached almost constant after immersion for 10 days, potentially availing to transport nutrients *in vivo* (Fig. S8). The ROS responsiveness and scavenging rate of R-AG hydrogel were verified by H_2O_2, as illustrated in Fig. 2B. Cylindrical R-AG hydrogels (Φ = 14mm × 2 mm) were immersed in water and H_2O_2 solution, respectively. Clearly, 1-h immersion in H_2O_2 almost totally disintegrated the hydrogel due to the sensitivity of borate ester bonds in the hydrogel backbone to H_2O_2, implying that R-AG hydrogel is ROS-responsive (Fig. 2Ba). Moreover, the concentration of B element in H_2O_2 solution was not only much higher than that in water but also increased over time, further confirming the responsive behavior of R-AG hydrogel to

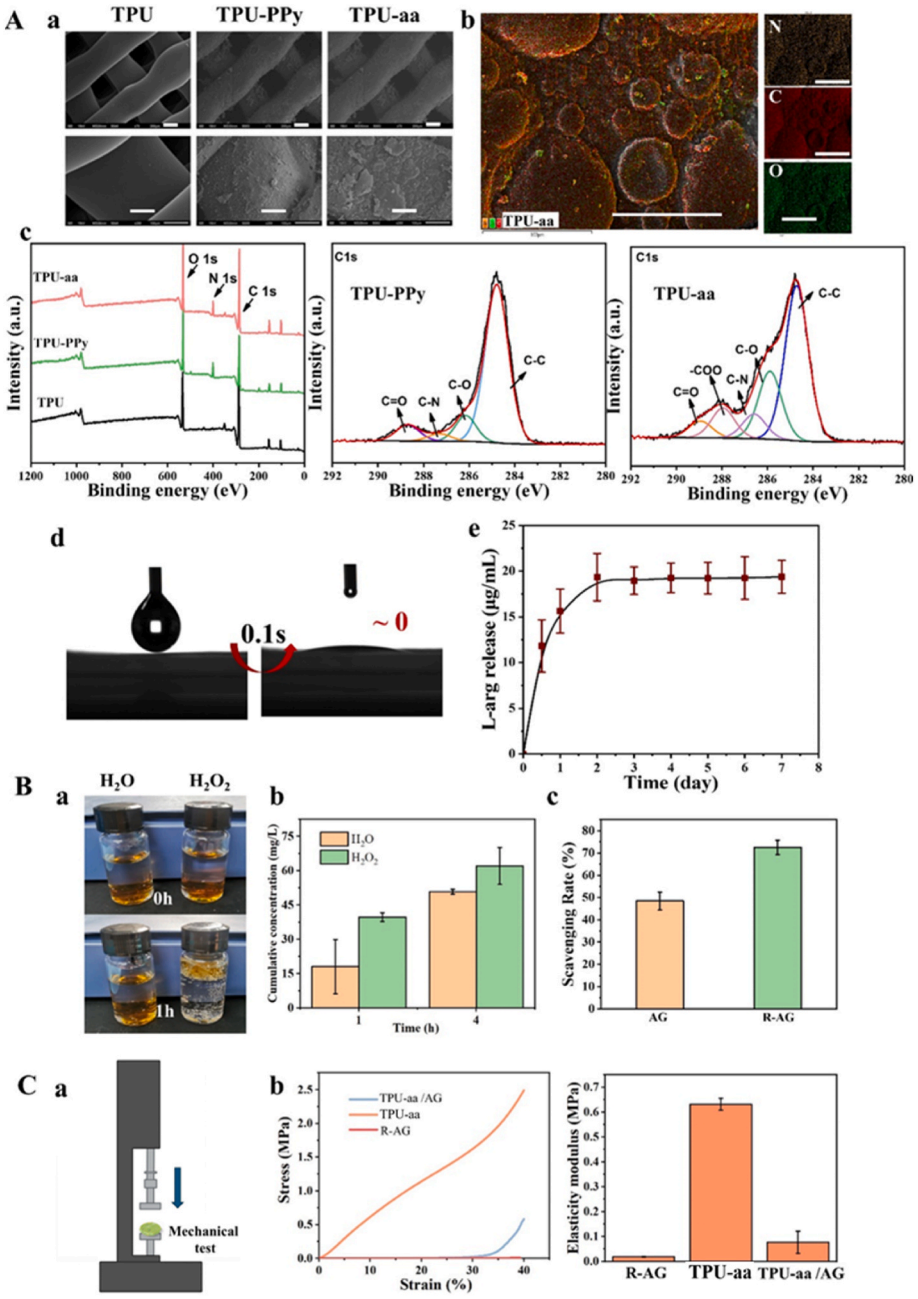

Fig. 2. A: (a) SEM images of TPU, TPU-PPy and TPU-aa scaffolds; (b) EDS mapping on TPU-aa scaffold corresponding to the SEM (scar bar: 100 μm); (c) XPS patterns including the deconvolution of C1s in scaffolds; (d) Images of water contact angle for TPU-aa at 0.1 s; (e) The release profile of L-arginine from the TPU-aa scaffold. B: (a) ROS-responsive behavior of R-AG hydrogel immersed in H_2O and H_2O_2; (b) Concentration of B element released from R-AG hydrogel in H_2O and 5 mM H_2O_2 soaking for different period, respectively; (c) H_2O_2 scavenging rates of AG and R-AG hydrogels. C: (a) The schematic of mechanical testing; (b) The stress-strain curves and elasticity modulus of R-AG hydrogels, TPU-aa scaffolds and TPU-aa/AG in compression.

ROS environment (Fig. 2Bb). By calculation, the scavenging rate of AG and R-AG hydrogels to H_2O_2 was 48.46 % and 72.54 %, respectively (Fig. 2Bc), because the –CHO in AG hydrogel could be oxidized into –COOH by H_2O_2, while the co-existence of –CHO and B-O groups in R-AG hydrogel could consume more H_2O_2. The interconnective pores in TPU-aa scaffold facilitates the infiltration of R-AG hydrogel precursor under negative pressure, thus the TPU-aa/AG hybrid hydrogel consisted by TPU-aa scaffold with R-AG hydrogel interpenetration after cross-linking was obtained, as can be seen from the cross section of TPU-aa/AG in Fig. S9. Also, we carried out the mechanical test for each group. (Fig. 2Ca). The compressive stress-strain curve of TPU-aa/AG was compared with those of TPU scaffold and R-AG hydrogel, apparently, the introduction of R-AG hydrogel made the TPU-aa/AG hybrid hydrogel present a typical viscoelastic behavior different from the TPU-aa scaffold, while the compressive modulus of TPU-aa/AG is lower than that of the TPU-aa scaffold due to the buffering effect of the surface hydrogel but notably greater than that of R-AG hydrogel (Fig. 2Cb). Mechanical tests indicated the R-AG hydrogel could not only bear a 500 g weight without distinct structural collapse, but also immediately recover to its original state upon removing the weight, demonstrating excellent resilience (Fig. S6). The recovery curves of the TPU-aa scaffold and the R-AG hydrogel after loading withdrawal in Fig. S10 display that due to the inevitable plastic deformation and internal friction, TPU-aa scaffold shows a poor hysteresis loop curve despite the high modulus, while the hysteresis loop of R-AG hydrogel is well enclosed owing to its excellent resilience. The force distribution in TPU-aa scaffold, R-AG

hydrogel and TPU-aa/AG hybrid hydrogel under compression was comparatively analyzed through FE simulation (Fig. S11). For normal stress of TPU-aa scaffold, the von Mises stress contour was higher and denser, implying that the stress was distributed concentration within it, while R-AG hydrogel under compression displayed a more even stress distribution but a bigger deformation compared to TPU-aa scaffold due to its low stiffness. In comparison, the stress distribution of TPU-aa/AG became more uniform, and the deformation condition is obviously

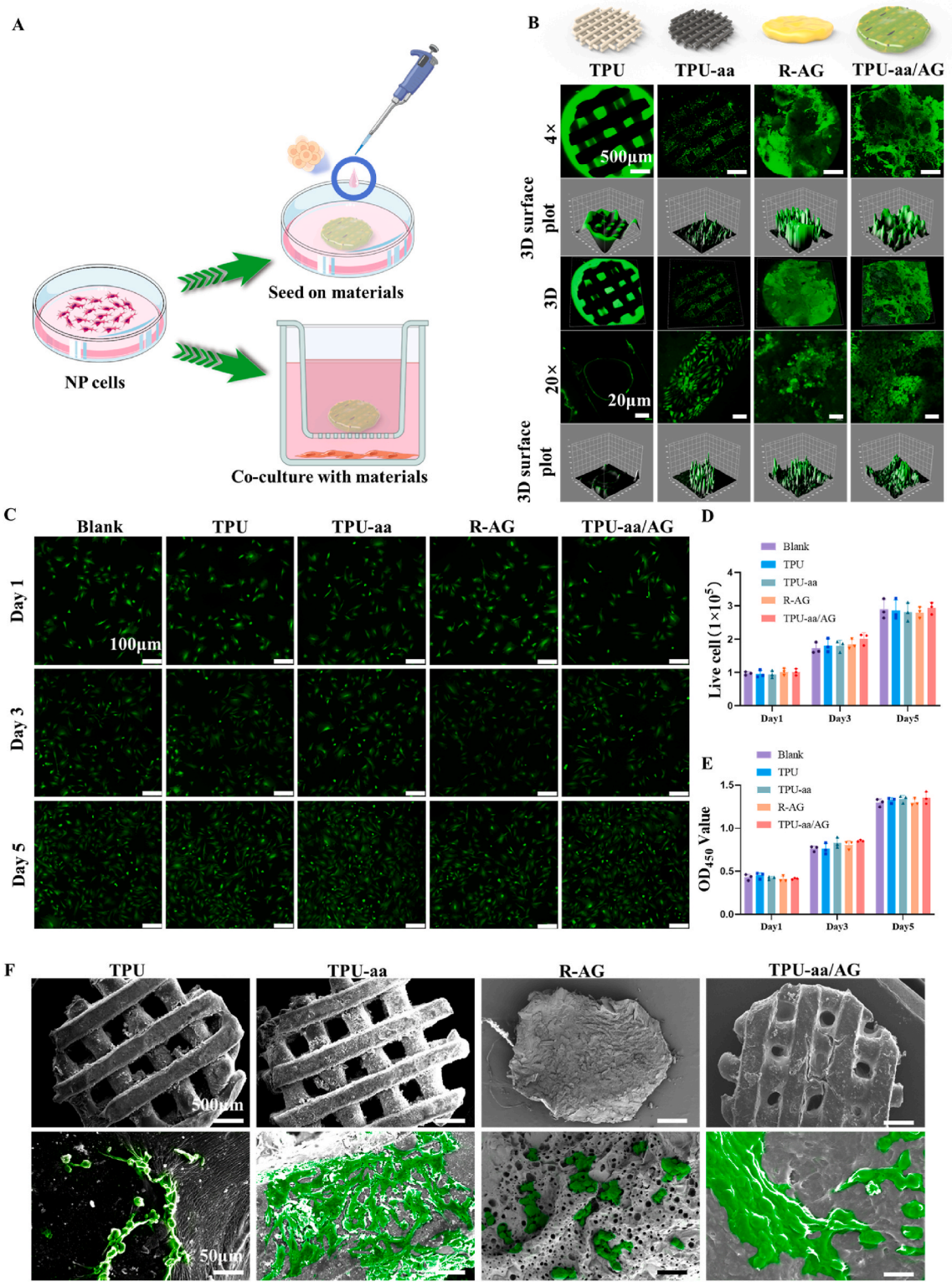

Fig. 3. A: Schematic illustration of two distinct cell co-culture methods on the materials. B: Live/dead staining of cells directly seeded onto the different material groups (4 × scale bar: 500 μm, 20 × scale bar: 20 μm). C: Live/dead staining of cells co-cultured with the materials (scale bar: 100 μm). D: Quantification of cell number at 1, 3, and 5 days. E: CCK-8 assay results at 1, 3, and 5 days. F: SEM images of cells seeded on the materials (green indicates cells, scale bar for top images: 500 μm, scale bar for bottom images: 50 μm).

improved. For shear stress, the TPU-aa/AG showed less deformation than TPU-aa scaffold and R-AG hydrogel. Therefore, the hybrid TPU-aa/AG system and R-AG hydrogel were endowed with enhanced stiffness and stress distribution. The FE analysis further corroborates the results of the *in vitro* compression tests. The hydrogel composite scaffold system, TPU-aa/AG, demonstrated an effective stress dissipation effect. Such a configuration may be more suitably applied in intervertebral disc repair due to its ability to alleviate stress concentrations.

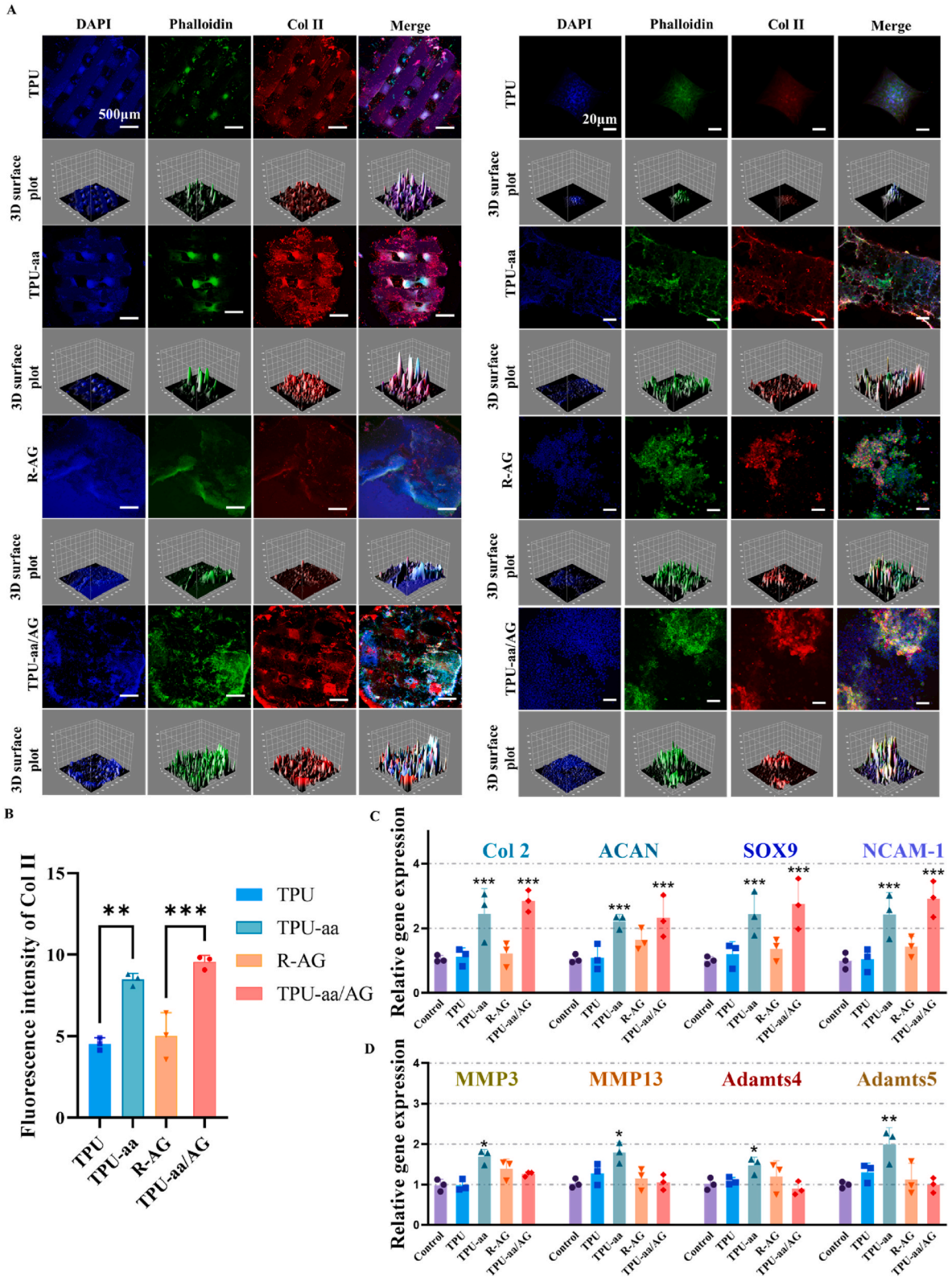

Fig. 4. Immunofluorescent staining and gene expression analysis of cells seeded on biomaterials. (A) Immunofluorescent staining of cells on the materials (left: 4 × magnification, scale bar: 500 μm; right: 20 × magnification, scale bar: 20 μm). (B) Quantitative analysis of type II collagen fluorescence in each material groups. (C) Expression of genes related to ECM synthesis and nucleus pulposus markers. (D) Expression of genes associated with ECM degradation.

3.2. Biocompatibility and cytotoxicity evaluation

Excellent biocompatibility and cellular adhesion are fundamental for tissue engineering and regenerative applications of materials [31]. Previous research demonstrated that surface modification to enhance the roughness of TPU scaffold could lead to improved cell adhesion [32,33]. Nucleus pulposus (NP) cells were seeded and co-cultured on four different materials to assess their biocompatibility and cytotoxicity (Fig. 3A). As shown in Fig. 3B, TPU's smooth surface hindered cell adhesion. In contrast, PPy-modified TPU scaffolds in TPU-aa and TPU-aa/AG groups showed good cell adhesion. The R-AG hydrogel allowed cell growth but failed to achieve proper spreading and pseudopodia formation. Co-culture assays (Fig. 3C) revealed no significant cytotoxicity among all material groups. Following rat tail intervertebral disc implantation of materials, histological analyses of the heart, liver, spleen, lungs, and kidneys revealed no organ toxicity (Fig. S12). Cell counting and CCK-8 assays supported their proliferation in all material groups absent of toxicity during 5 days (Fig. 3D and E). The SEM observations (Fig. 3F) of NP cells seeded onto each material were aligned with fluorescent staining findings. Minimal cells were visible on TPU scaffold due to the poor cell adhesion, while good adhesion, spreading, and growth of cells were observed on both TPU-aa and TPU-aa/AG groups. But cells on R-AG hydrogel poorly spread featured by spherical morphologies.

3.3. In vitro biological effects of mito-engine

Recent study has demonstrated that exogenous supplementation of amino acids involved in the tricarboxylic acid cycle could promote bone repair and extracellular matrix (ECM) synthesis [34]. More specifically, L-arginine and its downstream metabolic breakdown products, such as polyamines and glutamine, have been reported able to promote ECM synthesis and participate in cellular energy metabolism [11,35,36]. Here, immunofluorescent staining of cells cultured on various materials revealed that the TPU-aa and TPU-aa/AG groups exhibited a significant increase in collagen II (Col 2) fluorescence intensity compared to the unmodified TPU and R-AG groups (Fig. 4A and B), suggesting the promoted ECM collagen synthesis, which is an essential prerequisite for intervertebral disc tissue repair. Then the cells co-cultured with the four material groups were further digested to extract their RNA, aiming to assess the expression levels of NP marker genes. Just as Fig. 4C shows, the traditional marker genes including *Col 2*, *ACAN*, SRY-box transcription factor 9(*SOX9*), and neural cell adhesion molecule-1(*NCAM-1)* displayed a significant upregulation in TPU-aa and TPU-aa/AG groups, consistent with the above immunofluorescence findings.

In the context of IDD, the balance between anabolic and catabolic processes is crucial. We then investigated the expression levels of catabolic metabolism-associated genes, including matrix metalloproteinase-3 (*MMP3*), matrix metalloproteinase-13 (*MMP13*), a disintegrin and metalloproteinase with thrombospondin motifs-4 (*Adamts4*), and a disintegrin and metalloproteinase with thrombospondin motifs-5 (*Adamts5*). During IDD, *MMP*-related genes participate in the degradation of various collagenous elastin [37,38]. Similarly, *Adamts* primarily contributes to the degradation of proteoglycans. The proteoglycan breakdown in turn, results in the structural and functional damage of intervertebral disc tissues [39]. Interestingly, we found these catabolic metabolism-associated genes showed varied levels of upregulation in NP cells co-cultured with TPU-aa (Fig. 4D). This suggested a state of heightened metabolic activity, characterized by simultaneous and elevated rates of ECM synthesis and degradation. Such a high-energy consumption process, while indicative of active repair, could potentially lead to an imbalance in ECM homeostasis.

Comparatively, in the TPU-aa/AG group, we observed a more moderated expression of these catabolic genes. This implied that the integration of the antioxidative hydrogel within the TPU-aa scaffold potentially mitigated the intense metabolic activity, thereby fostering a more balanced ECM turnover. This finding underscored the significance of incorporating the hydrogel as a coolant into the TPU-aa scaffold, as it seems to provide a more conducive environment for controlled ECM synthesis and degradation, crucial for sustainable IDD repair.

3.4. RNA-sequencing of mito-engine

To elucidate the biological effects observed in the TPU-aa/AG group, we conducted transcriptome sequencing for both the TPU-aa/AG group and the IDD negative control group. Transcriptome sequencing (RNA-seq) is a high-throughput gene expression analysis method that detects all RNA molecules produced during transcription processes in cells or tissues, thus aiding our understanding of gene expression patterns and regulatory mechanisms [40]. In the heatmap of Fig. 5A, we performed clustering analysis on differentially expressed genes between the two groups, identifying 3,955 significantly differentially expressed genes. Among them, the mTOR gene was considered one of the most remarkably upregulated genes in TPU-aa/AG group (Fig. 5B). Enriching the differentially expressed genes in the GO database revealed that most upregulated genes in the TPU-aa/AG group were associated with organelle structure and function and positive biological effects (Fig. 5C and D). In the CC, MF, and BP subgroups (Fig. 5E–G), the majority of genes enriched in CC indicated enhanced organelle and membrane-related functions; while in the MF pathway-enriched genes, the most significant differences were found in ATP binding-related genes within the TPU-aa/AG group, with many others involved in nucleotide and protein binding; and the genes enriched in the BP pathway suggested a significant upregulation of those related to positive regulation of metabolic processes and metabolic process-associated genes. These findings align well with our initial intention in designing the TPU-aa/AG material, that is, promoting cell synthesis and energy metabolism through the provision of exogenous amino acid by a bioenergetic scaffold, ultimately achieving tissue repair.

3.5. Mito-engine regulated the MRC function and increased the $\Delta\Psi m$

The high-throughput RNA-seq provided a foundation for understanding the biological effects of TPU-aa/AG at the gene level, next we investigated the specific efficacy of TPU-aa/AG on energy metabolism at the cellular level. The electron transport chain (ETC), part of the respiratory chain, primarily consists of four large complexes: Complex I (NADH dehydrogenase), Complex II (succinate dehydrogenase), Complex III (cytochrome *bc*1 complex), and Complex IV (cytochrome *c* oxidase) [41]. Electrons can be transferred through these complexes by means of auxiliary factors such as Coenzyme Q and cytochrome C. The transfer of electrons is accompanied by the release of energy, driving protons to move from the mitochondrial matrix side to the intermembrane space side, forming the mitochondrial membrane potential [42]. When the mitochondrial membrane potential is sufficiently high, the proton backflow will release energy, causing conformational changes in the F_1 portion of ATP synthase, promoting the synthesis of ATP from ADP and inorganic phosphate (Pi). This process supplies energy for cellular activities. However, under external inflammation and excessive ROS conditions, the excess of ROS will disrupt the integrity of the inner and outer mitochondrial membranes, leading to increased membrane permeability, which often weakens the proton gradient and reduces the mitochondrial membrane potential. As a result, the cellular oxidative phosphorylation will be inhibited due to reduced mitochondrial membrane potential and damaged respiratory chain, further affecting the proton backflow and ATP synthase activity. Ultimately, this reduces cellular ATP production, leading to cellular stress responses and apoptosis [43,44]. As such, the implantation of TPU-aa/AG as the "Mito-engine" can first "cool-down" the inflammatory environment, thereby clearing both external and intracellular excessive ROS, restoring the mitochondrial membrane potential, and breaking the vicious cycle caused by the inflammatory environment, finally allowing cells to regain

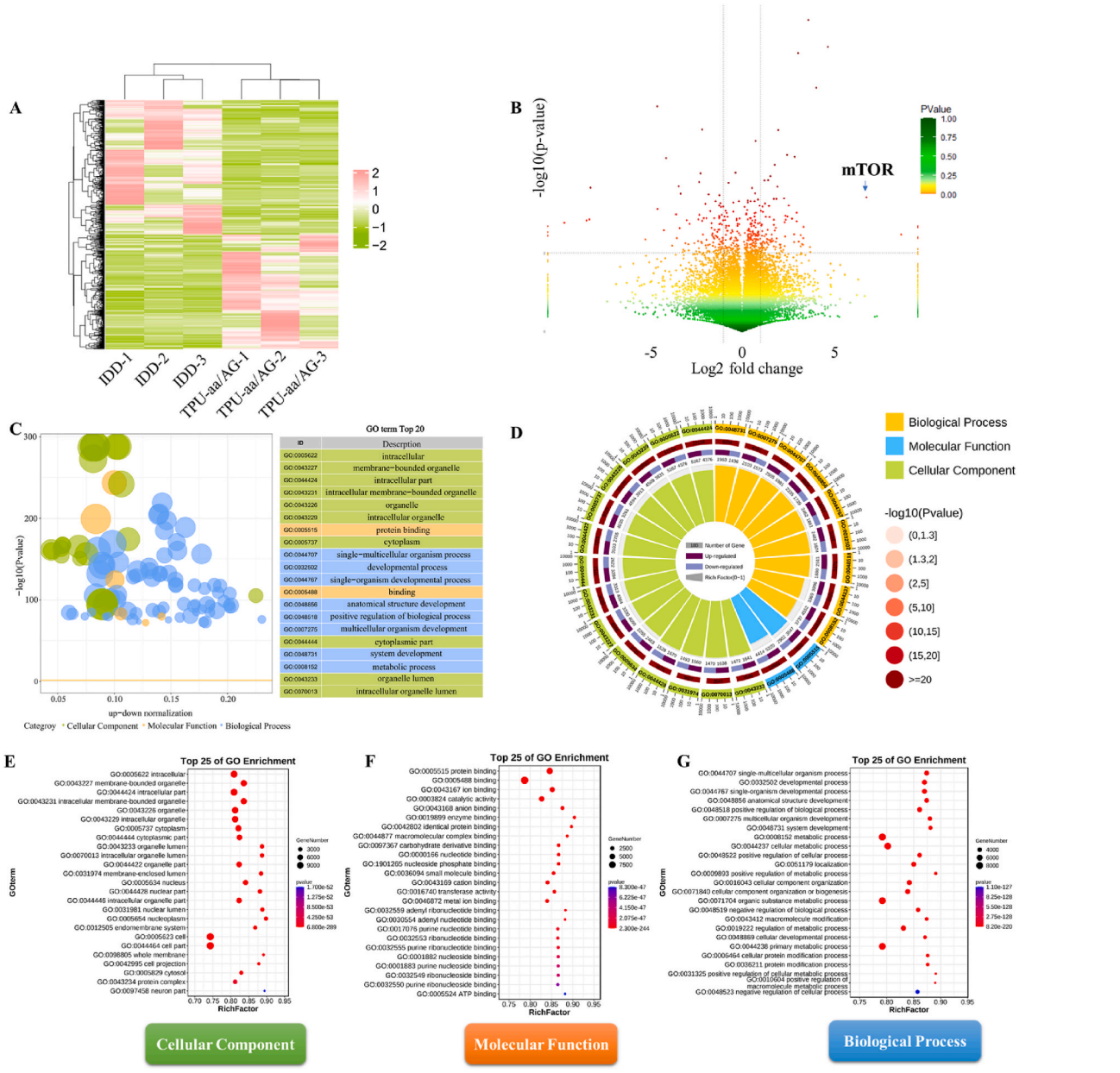

Fig. 5. RNA sequencing revealed a significant upregulation of cellular energy metabolism and synthesis-related pathways in the TPU-aa/AG group. (A) Heatmap of differential gene expression between IDD and TPU-aa/AG groups; (B) Volcano plot of upregulated and downregulated genes, with mTOR notably upregulated in the TPU-aa/AG group. (C) Bubble chart of z-score from GO enrichment analysis. (D) Circle diagram of GO enrichment analysis. Enrichments in GO pathways separately shown in (E) CC, (F) MF, and (G) BP subgroups.

normal energy metabolism capabilities (Fig. 6A).

In this study, oxygen consumption rate (OCR) technology was used to detect the oxygen consumption of different cell groups after 12-h intervention under H_2O_2-induced oxidative stress (Fig. 6B). As shown in Fig. 6C–E, H_2O_2 stimulation led to a decrease in basal respiration rate and an increase in proton leakage in cells, suggesting the MRC function inhibition of NP cells. However, treatments with TPU-aa, R-AG, and TPU-aa/AG groups could effectively reduce the H_2O_2-induced proton leakage and significantly restore the ATP production capacity. Subsequently, we assessed mitochondrial membrane potential in different cell groups using JC-1. JC-1 is a dual-emission fluorescent dye that exists as monomers and aggregates. At low mitochondrial membrane potentials, JC-1 exists as monomers emitting green fluorescence, while at high membrane potentials, it forms aggregates emitting red fluorescence [45]. We found that in the cells not treated with H_2O_2, the TPU-aa and TPU-aa/AG groups displayed higher red fluorescence intensities, which was also confirmed by flow cytometry. After H_2O_2 treatment, although all cell groups exhibited varying decrease in membrane potentials, the cells of TPU-aa/AG group still displayed a red fluorescence from aggregated JC-1, indicating that TPU-aa/AG maximally maintained the mitochondrial membrane potential under oxidative stress (Fig. 6F). Furthermore, we employed flow cytometry to verify the mitochondrial membrane potential in each group (Fig. 6G, **H**). Notably, under H_2O_2 stimulation, the TPU-aa L-arginine groups but failed to maintain the membrane potential comparable to the TPU-aa/AG group. This might be caused by the TPU-aa group providing amino acid for enhanced energy metabolism, but failing to effectively eliminate the external ROS environment; under sustained external ROS stimulation, cells inevitably experienced a decline in mitochondrial membrane potential and apoptosis. As for the R-AG group, despite the clearance of external ROS

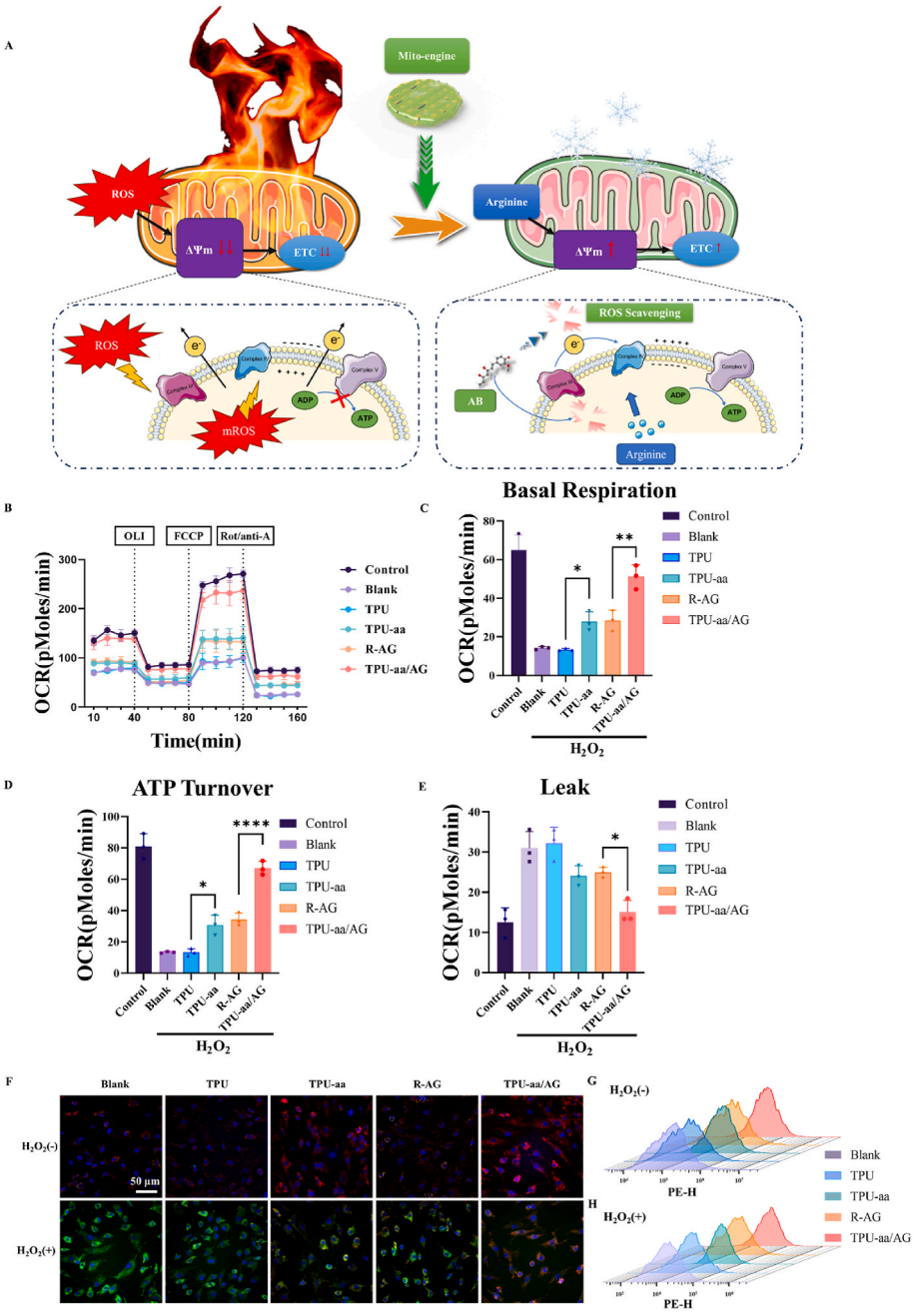

Fig. 6. The protective effect of "mito-engine" on cellular MRC. (A) Schematic illustration of "Mito-engine" rescuing cell membrane potential and attenuating ROS generation. (B) The OCR of NP cells treated with different groups. Parameter analysis, including (C) basal respiration, (D) ATP turnover, and (E) proton leakage, based on OCR results. (F) Representative fluorescent images of mitochondrial membrane depolarization interfered by H_2O_2 (100 μMol) analyzed by JC-1 staining (scale bar: 50 μm). Flow cytometry results of JC-1 staining for (G) the untreated and (H) H_2O_2-treated groups.

environment, the cells already damaged by external oxidative stress were still hard to regain increased membrane potential, resulting in a decrease in membrane potential. Consequently, the TPU-aa/AG group that integrated both ROS clearance and energy metabolism enhancement abilities, could not only remove the external oxidative stress environment promptly but also modulate the MRC function, restore the normal energy metabolism and finally demonstrate excellent reparative performance at cellular level.

3.6. Evaluation of ROS scavenging

Subsequently, we assessed the specific ROS scavenging efficacy among different groups. Intracellular ROS levels were detected using the DCFH-DA fluorescent probe, which could be oxidized by ROS, triggering a fluorescence reaction and enabling the measurement of ROS in cells and tissues. As observed, following H_2O_2 treatment, the fluorescence intensity significantly increased in the Blank, TPU, and TPU-aa groups, indicating high ROS levels. In contrast, the R-AG and TPU-aa/AG groups maintained lower fluorescence levels, demonstrating that R-AG and TPU-aa/AG effectively eliminated ROS at cellular level, thus resulting in an improved reparative environment (Fig. 7A and B). The corresponding morphological changes and damage extent of mitochondria were further observed by TEM. As shown in Fig. 7C, the lack of effective control over the external oxidative stress caused mitochondrial outer membrane swelling, inner membrane cristae rupture, and severe mitochondrial damage in the Blank, TPU, and TPU-aa groups. However, the R-AG

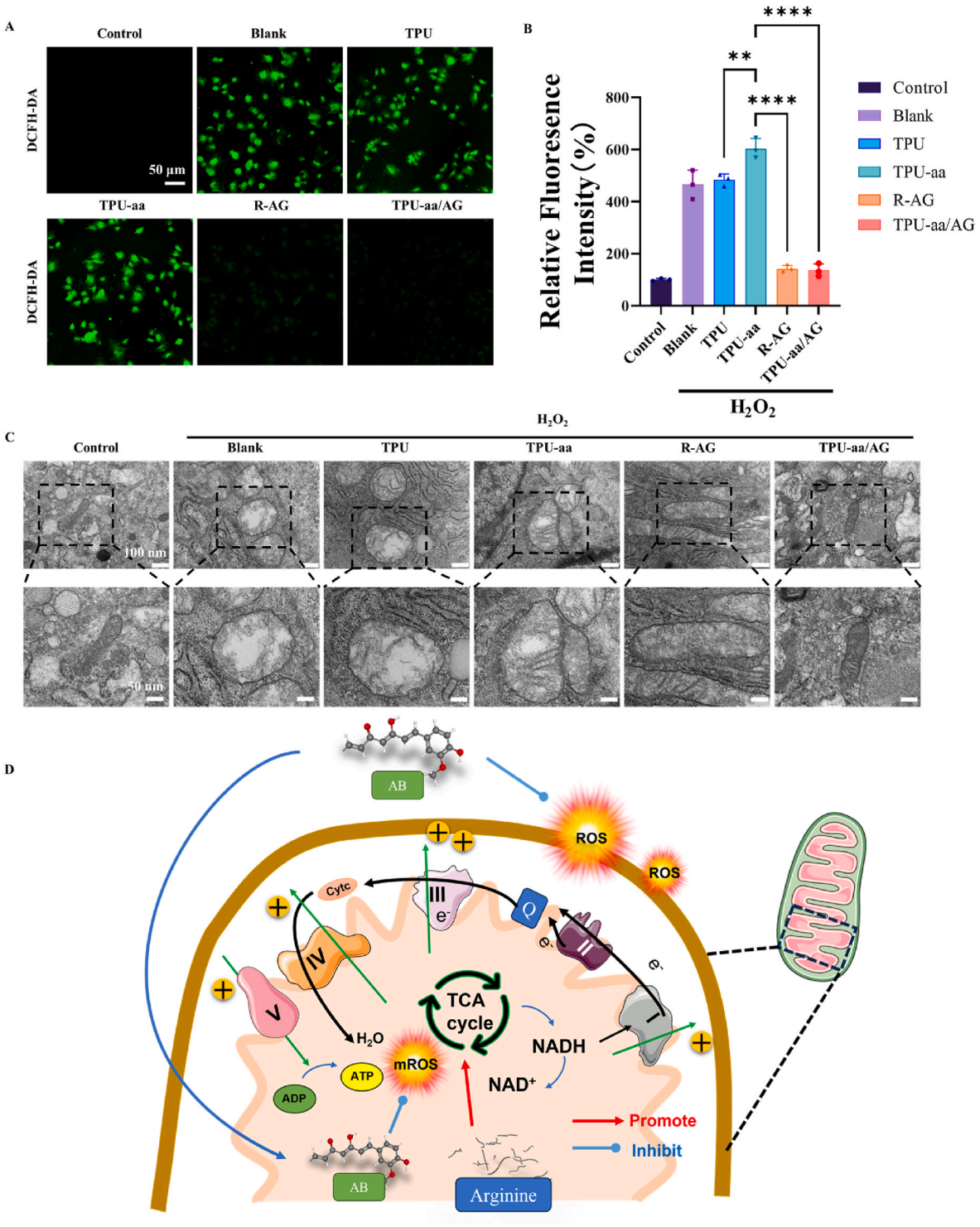

Fig. 7. The "mito-engine" capable of eliminating ROS to preserve the normal morphology of mitochondria under inflammatory conditions. (A) Fluorescent images of ROS in NP cells induced by 100 μMol H_2O_2 via DCFH-DA, scale bar: 50 μm. (B) The correspondingly relative fluorescence intensity. (C) The biological TEM images of the intracellular mitochondria intervened by H_2O_2 (scale bar for top images: 100 nm, scale bar for bottom images: 50 nm). (D) The schematic illustration to elucidate the mechanism of "mito-engine" rescuing the MRC, mitigating ROS, and maintaining intracellular mitochondrial morphology.

group exhibited partial mitochondrial swelling and mild inner membrane cristae damage. Remarkably, the TPU-aa/AG group almost had no mitochondrial swelling, but displayed clear mitochondrial structure and intact inner membrane cristae similar to the control group. Obviously, although the TPU-aa group likely provided a transient increase in mitochondrial membrane potential, its mitochondrial morphology was still severely compromised under external oxidative stress. In this regard, the mitochondria resembled an "energy engine" in an overloaded state, unable to maintain long-term supply of mitochondrial membrane potential. In contrast, the TPU-aa/AG group capable of "cooling-down" the external inflammatory oxidative stress, could maintain normal mitochondrial morphology, thereby effectively sustaining cellular energy supply.

Fig. 8 Radiological evaluation of each group *in vivo* treatment. (A) X-

ray, CT, 3D-CT reconstruction, and MRI images, (B) DHI, (C) Osteophyte volume across different material groups, and (D) MRI Pfirrmann classification.

Based on the above results, the potential mechanism underlying Mito-engine's reparative function for cells (Fig. 7D) was deduced as follows: the excessive intracellular and extracellular ROS were first cleared out by the ROS-responsive moieties in the TPU-aa/AG, then the material provided an optimal external environment for cells to restore normal mitochondrial membrane potential. Concurrently, the L-arginine supplied by the bioenergetic scaffold entered into the cells to promote the tricarboxylic acid cycle and enhance the energy synthesis under oxidative stress, ultimately restoring the normal energy metabolism for propelling the IDD repair.

3.7. Radiological evaluation of "mito-engine" for IDD treatment

Further *in vivo* studies were also conducted to confirm the therapeutic effect of TPU-aa/AG ("Mito-engine") on IDD. Fig. S13 shows the implantation surgery of different materials into rats, and the rats were ultimately divided into 6 groups: sham, IDD, TPU, TPU-aa, R-AG, and TPU-aa/AG. At 8 weeks post-surgery, radiographic examinations, including X-ray, CT, and MRI, were conducted on each group.

Based on previous research, intervertebral discs necessitate optimal mechanical environment, which imposes strict requirements on the mechanical properties of implants. Scaffold materials, in comparison to purely hydrogel-based materials, are more likely to maintain disc height in degenerated intervertebral discs [46–48]. X-ray images revealed a significant decrease in the disc height index (DHI) for the TPU, TPU-aa, and R-AG groups compared to the sham group, with no significant difference between the TPU, R-AG, and IDD groups. The TPU-aa group exhibited slightly increased disc height, suggesting that its rigid scaffold structure provided some support for maintaining disc height. The TPU-aa/AG group was able to maintain disc height more effectively, showing only a slight reduction compared to the sham group, indicating that by combining a flexible hydrogel with a rigid scaffold structure, the mechanically biomimetic TPU-aa/AG scaffold preferred to provide the natural mechanical environment required by the intervertebral discs of rats (Fig. 8A and B). However, the exclusive use of rigid scaffold materials might lead to issues such as stress shielding or rigid cutting due to the mismatch in stress contact interfaces, as well as scaffold subsidence, probably exacerbating local inflammation, promoting osteophyte formation, and affecting the regeneration and repair of intervertebral discs [49]. In the CT examination, 3D reconstruction of rat tail vertebrae and quantitative analysis of osteophytes produced in the intervertebral space showed an increased number of osteophytes in the TPU, TPU-aa, and R-AG groups compared to the sham group. Notably, the TPU and TPU-aa groups had even more osteophytes than the IDD group, possibly caused by the mismatch of rigid scaffold structure with disc stress or excessive stress concentration, thus leading to more rigid friction and micromotion between the intervertebral space scaffold and the adjacent endplates, accelerating disc inflammation, stimulating osteophyte formation, and deteriorating disc degeneration. Although the R-AG group eliminated ROS in the IDD, it was hard to provide sufficient support, leading to osteophyte formation under biomechanical stress. However, the TPU-aa/AG group significantly reduced the osteophyte production compared to the IDD group, achieving superior reparative performance

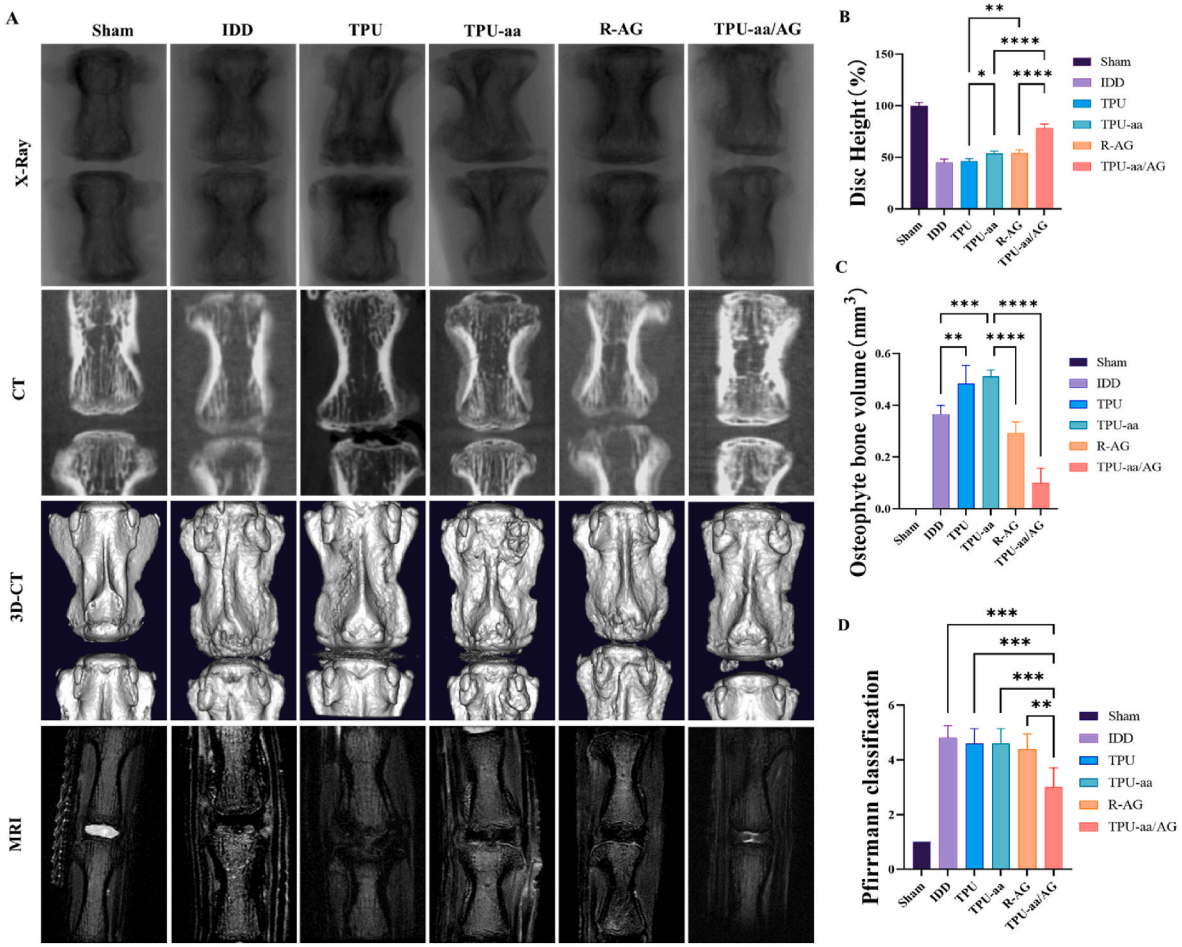

Fig. 8. Radiological evaluation of each group *in vivo* treatment. (A) X-ray, CT, 3D-CT reconstruction, and MRI images, (B) DHI, (C) Osteophyte volume across different material groups, and (D) MRI Pfirrmann classification.

(Fig. 8A–C). Since the extracellular matrix in the NP of intervertebral discs primarily consists of collagen fibers, proteoglycans, and water, the efficacy of *in vivo* disc repair can be assessed based on the signal intensity variations in T2-weighted MRI [50,51]. MRI examination demonstrated that the TPU, TPU-aa, and R-AG groups lacked high signal intensity in the intervertebral space on T2-weighted images, indicating a loss of water content and proteoglycan components. In contrast, the TPU-aa/AG group better retained intervertebral space hydration, resulting in lower Pfirrmann classification (Fig. 8A–D).

3.8. Histological evaluation of "mito-engine"

Histological staining of *in vivo* experiments revealed that, although the TPU and TPU-aa groups could provide support to the intervertebral space, no discernible gelatinous NP tissue remained within their intervertebral discs. Instead, extensive fibrotic tissue surrounding the material was observed, similar to the IDD group, indicating disc degeneration. In the R-AG group, the hydrogel system preserved a small amount of NP-like gelatinous tissue within the intervertebral disc. However, compared to the Sham group, substantial NP tissue loss occurred in R-AG group, and the demarcation between the NP and annulus fibrosus was indistinct. But as for TPU-aa/AG group, its scaffold structure offered an excellent support, while the infiltrated hydrogel in the scaffold maximally kept the NP tissue within the intervertebral disc, and a clear boundary existed between the NP and annulus fibrosus (Fig. 9A), resulting in a lower histological score compared to IDD and other groups (Fig. 9B and C). Overall, the TPU-aa/AG group demonstrated a superior regenerative effect among all material groups.

3.9. The "mito-engine" promotes tissue repair through the activation of mTOR

In the above high-throughput sequencing, we observed a significant upregulation of the mTOR gene in the TPU-aa/AG group. The mammalian target of rapamycin (mTOR) is a serine/threonine protein kinase that plays a crucial role in regulating cell growth, proliferation, and metabolism [52]. Previous study showed that L-arginine could directly promote the assembly and activation of mTORC1 on lysosomal membranes. L-arginine stimulates mTORC1 phosphorylation, which in turn enhances the phosphorylation of downstream p70 S6K, ultimately promoting cell growth and proliferation [53]. A recent investigation revealed that mTORC1 protects macrophages from mycobacteria-induced death by promoting mitochondrial energy augmentation [54]. Consequently, we hypothesize that a "mito-engine" releases L-arginine to stimulate mTORC1, elevating the mitochondrial membrane potential and promoting the restoration of energy metabolism in degenerated intervertebral disc cells. This process may ultimately facilitate the ECM production to repair the intervertebral disc.

To test this hypothesis, we assessed mTOR gene expression in various groups using quantitative real-time PCR (qrt-PCR). In line with the sequencing results, both the TPU-aa/AG and TPU-aa groups exhibited *mTOR* gene upregulation (Fig. 10A). We then evaluated the phosphorylation status of mTOR protein and its downstream molecule p70 S6K in each group using Western blotting. Consistent with the gene expression data, the S2448 site of mTOR in the TPU-aa/AG and TPU-aa groups showed significantly increased phosphorylation, accompanied by a notable upregulation of phosphorylated p70 S6K (Fig. 10B). Moreover, immunofluorescence staining of mTOR in the cells co-cultured with different materials revealed enhanced fluorescent signal intensity in the cells co-cultured with TPU-aa/AG and TPU-aa in comparison to other groups (Fig. 10C and D). We further performed immunohistochemical staining of tissue sections from *in vivo* experiments. We initially assessed COL2 expression in different groups and observed a significant increase in the TPU-aa/AG group, approaching the level in the normal group. Although the TPU-aa group also exhibited an upregulation of COL2 expression, it did not reach the level observed in the TPU-aa/AG group. These *in vivo* results suggested that even though the TPU-aa group could promote the ECM synthesis to some extent, its inability to eliminate external reactive ROS still hindered the optimal reparative effects. While the R-AG group displayed higher COL2 level than the TPU and IDD groups but still had a significant gap from the TPU-aa/AG group, because the R-AG group was able to control the external ROS but unable to promote the energy metabolism recovery in damaged cells, resulting in suboptimal ECM synthesis (Fig. 10E and F). Immunohistochemical analysis of mTOR revealed significantly upregulated mTOR expression in both the TPU-aa and TPU-aa/AG groups, supporting our hypothesis of these materials promoting mTOR expression through L-arginine, thereby enhancing mitochondrial membrane potential and restoring energy metabolism in degenerated tissues (Fig. 10E–G).

In summary, "mito-engine" offered a dual approach to promote intervertebral disc regeneration. On one hand, the bioenergetic active scaffold structure (TPU-aa) released L-arginine into the degenerated disc environment. The cells then actively transported and internalized L-L-arginine, which in turn activated the mTOR pathway and its downstream substrate S6K. This activation restored the mitochondrial membrane potential in the degenerated cells, enhanced the ETC activity, and subsequently reestablished the normal energy metabolism in the damaged cells. On the other hand, the intelligent responsive diagnostic and scavenging properties of the R-AG enabled effective removal of ROS from the extracellular environment, thereby creating favorable conditions for cellular recovery. Simultaneously, the R-AG prevented excessive mitochondrial activation that could cause an overproduction of mitochondrial ROS (mROS). This mechanism maintained relatively low dynamic equilibrium of ROS within the system, ultimately resulting in exceptional regenerative outcome, as illustrated in Fig. 10H.

4. Conclusions

In this study, we developed a "mito-engine" which was a bioenergetic active scaffold containing L-L-arginine and infused it with an intelligent responsive hydrogel that exhibited ROS-responsive scavenging properties for intervertebral disc degeneration repair. Both *in vitro* and *in vivo* experiments demonstrated that the mito-engine effectively elevated the mitochondrial membrane potential in NP cells and regulated the ROS levels, thus enhancing the ETC function, reducing the proton leakage, preventing the oxidative damage, and ultimately stimulating the regenerative processes in the degenerated intervertebral disc. We believe that the "Mito-engine" holds a promise as a novel strategy for treating IDD and has potential applications in other degenerative diseases associated with MRC dysfunction.

Ethics approval and consent to participate

This study was conducted in accordance with the guidelines approved by the Institutional Animal Care and Use Committee of West China Hospital, Sichuan University (approval number: 20220718002).

Data availability statement

The data that support the findings of this study are available on reasonable request from the corresponding authors.

CRediT authorship contribution statement

Juehan Wang: Writing – original draft, Funding acquisition, Formal analysis, Data curation. **Yulin Jiang:** Writing – original draft, Resources, Formal analysis, Data curation. **Ce Zhu:** Investigation, Funding acquisition. **Zheng Liu:** Visualization. **Lin Qi:** Software. **Hong Ding:** Validation, Data curation. **Jing Wang:** Investigation. **Yong Huang:** Resources. **Yubao Li:** Conceptualization. **Yueming Song:** Supervision. **Ganjun Feng:** Supervision, Project administration, Funding acquisition. **Li Zhang:** Writing – review & editing, Supervision. **Limin Liu:**

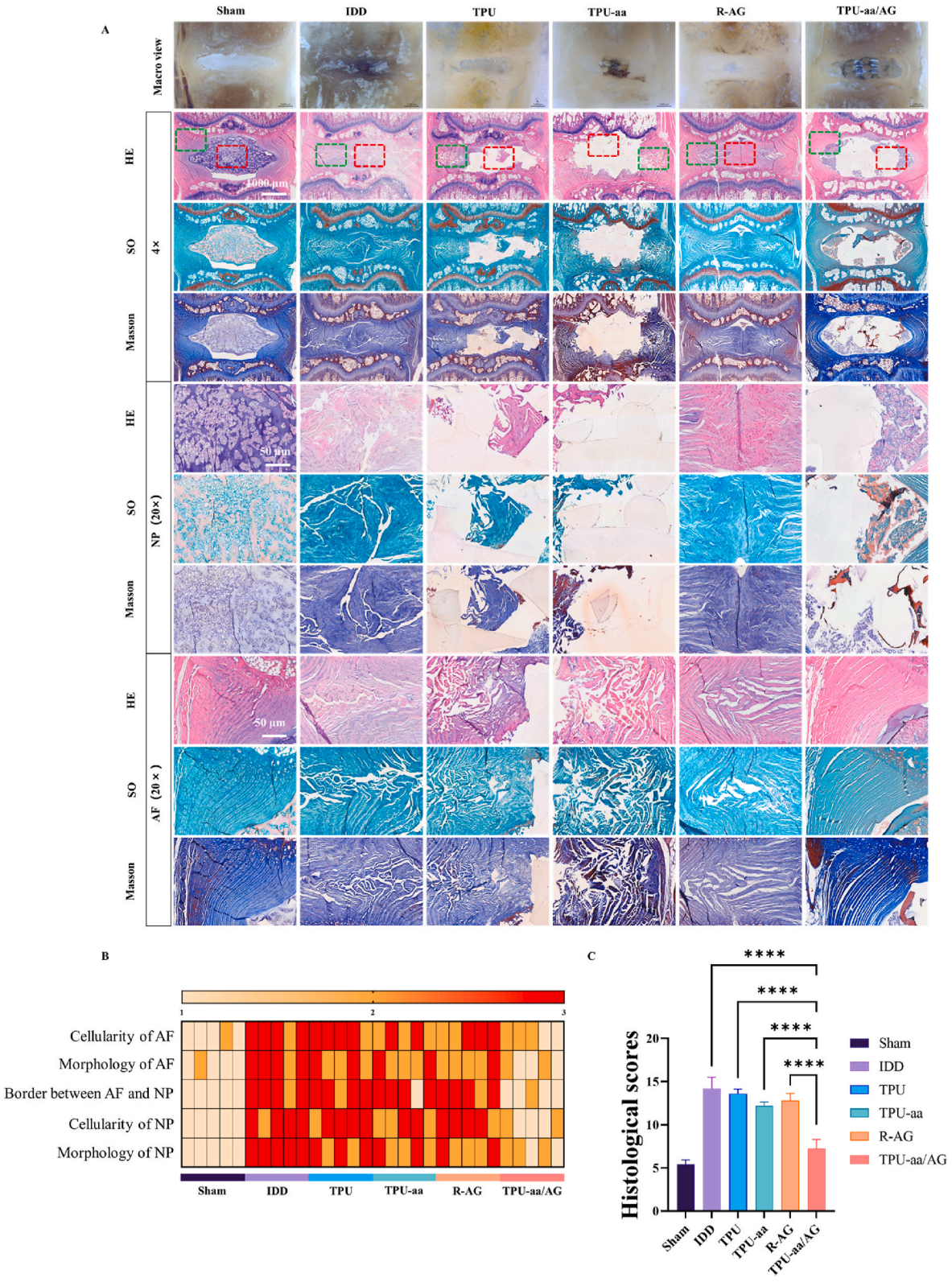

Fig. 9. Mito-engine promoted IVD regeneration in IDD rats. (A) Macroscopic photographs, H&E, Safranin O/Fast Green, and Masson's trichrome staining images of each group, the red box represents the 20 × magnified NP area, while the green box represents the 20 × magnified AF area in the 4 × images. 4 × scale bar: 1000 μm, 20 × scale bar: 50 μm. (B) The individual and (C) the cumulative histological scores post postoperatively indicated the statistically significant differences of the TPU-aa/AG group compared with the IDD group.

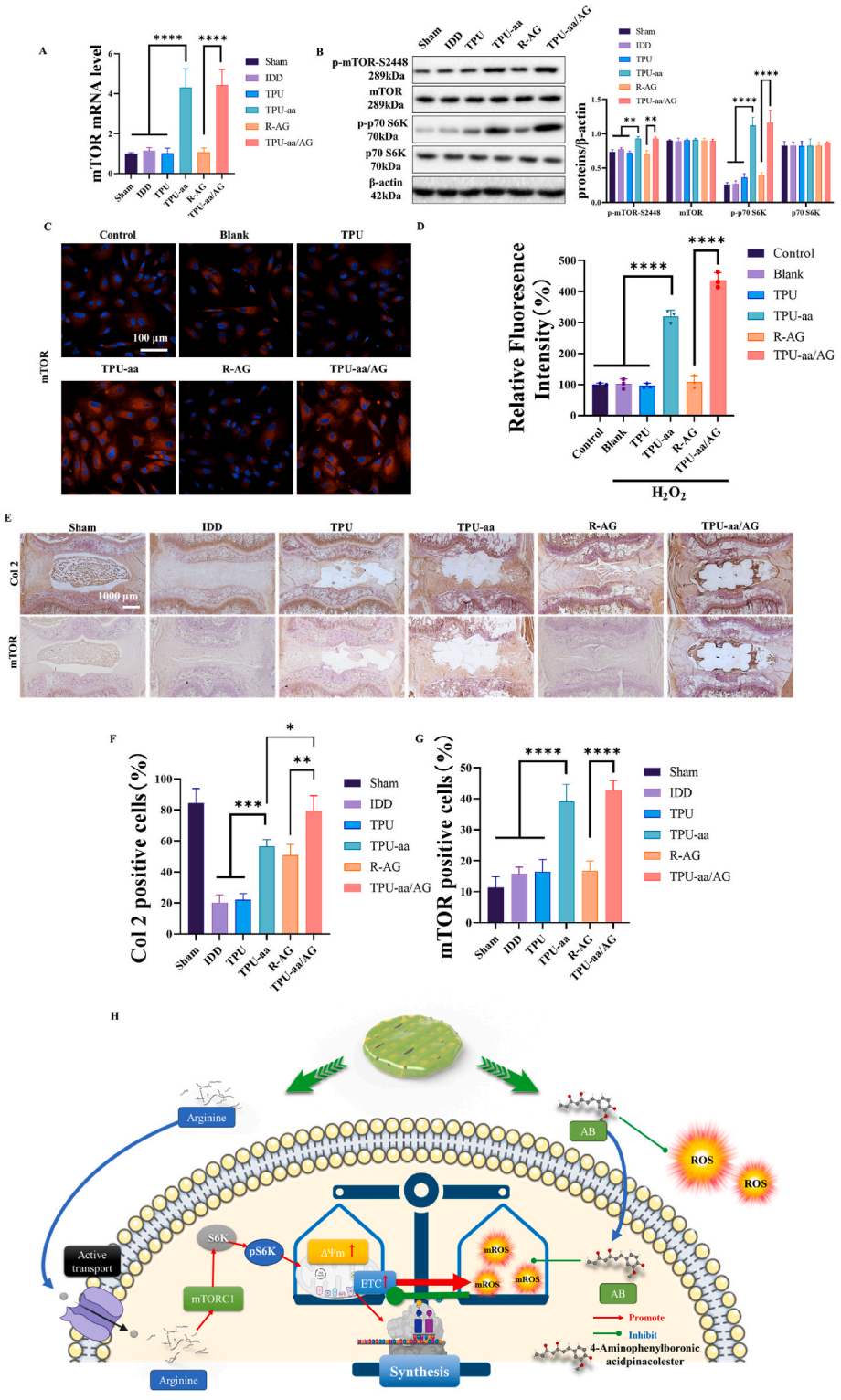

Fig. 10. (A) Expression levels of the mTOR gene in different groups. (B) Expression levels of mTOR-associated proteins in different groups. (C) Fluorescent images of mTOR in co-cultured cells across all groups, scale bar: 100 μm. (D) Quantitative analysis of mTOR fluorescence intensity in each group. (E) Immunohistochemical images of COL2 and mTOR for each group, scale bar: 1000 μm. (F) Quantification of COL2-positive cells in immunohistochemistry. (G) Quantification of mTOR-positive cells in immunohistochemistry. (H) Schematic illustration of the "mito-engine" promoting intervertebral disc repair by activating the mTOR pathway.

Supervision, Project administration, Funding acquisition.

Declaration of competing interest

The authors declare that they have no known competing financial interests or personal relationships that could have appeared to influence the work reported in this paper.

Acknowledgements

The authors acknowledge the National Natural Science Foundation of China (82172495, 82260431,82072434,82372453); Project funded by China Postdoctoral Science Foundation(2023M732469); Sichuan University Postdoctoral Interdisciplinary Innovation Fund (JCXK2205); Projects of the Science and Technology Department of Sichuan Province (2022ZDZX0029,MZGC20230019); the 1·3·5 project for disciplines of excellence Clinical Research Incubation Project, West China Hospital, Sichuan University (2021HXFH003). The authors would also like to thank Xi Wu (Analytical & Testing Center, SCU) for his help with ICP testing, and Yan Wang, Xiangyi Ren, Cong Li and Hongying Chen from the Core Research Facility of West China Hospital, Sichuan University, for their kind assistance with the cell/molecular experiments. We also thank Lei Wu from Histology and Imaging Platform, Core Facilities of West China Hospital for micro-CT scanning and Li Li, Chunjuan Bao and Fei Chen of the Institute of Clinic Pathology, Sichuan University, for dealing with histology staining.

Appendix A. Supplementary data

Supplementary data to this article can be found online at https://doi.org/10.1016/j.bioactmat.2024.05.044.

References

[1] Y. Song, S. Lu, W. Geng, X. Feng, R. Luo, G. Li, et al., Mitochondrial quality control in intervertebral disc degeneration, Exp. Mol. Med. 53 (7) (2021) 1124–1133.
[2] Z. Lin, H. Wang, J. Song, G. Xu, F. Lu, X. Ma, et al., The role of mitochondrial fission in intervertebral disc degeneration, Osteoarthritis Cartilage 31 (2) (2023) 158–166.
[3] M.M. Klemmensen, S.H. Borrowman, C. Pearce, B. Pyles, B. Chandra, Mitochondrial dysfunction in neurodegenerative disorders, Neurotherapeutics 21 (1) (2024) e00292.
[4] X. Chen, Y. Ji, R. Liu, X. Zhu, K. Wang, X. Yang, et al., Mitochondrial dysfunction: roles in skeletal muscle atrophy, J. Transl. Med. 21 (1) (2023) 503.
[5] J. Bai, Y. Zhang, Q. Fan, J. Xu, H. Shan, X. Gao, et al., Reactive oxygen species-scavenging scaffold with rapamycin for treatment of intervertebral disk degeneration, Adv. Healthcare Mater. 9 (3) (2020) e1901186.
[6] L. Yang, B. Bhujel, Y. Hou, J. Luo, S.B. An, I. Han, et al., Effective modulation of inflammation and oxidative stress for enhanced regeneration of intervertebral discs using 3D porous hybrid protein nanoscaffold, Adv. Mater. 35 (41) (2023) e2303021.
[7] H. Zhou, J. He, R. Liu, J. Cheng, Y. Yuan, W. Mao, et al., Microenvironment-responsive metal-phenolic network release platform with ROS scavenging, anti-pyroptosis, and ECM regeneration for intervertebral disc degeneration, Bioact. Mater. 37 (2024) 51–71.
[8] Y. Wang, Y. Wu, B. Zhang, C. Zheng, C. Hu, C. Guo, et al., Repair of degenerative nucleus pulposus by polyphenol nanosphere-encapsulated hydrogel gene delivery system, Biomaterials 298 (2023) 122132.
[9] C.R. Morris, J. Hamilton-Reeves, R.G. Martindale, M. Sarav, J.B. Ochoa Gautier, Acquired amino acid deficiencies: a focus on arginine and glutamine, Nutr. Clin. Pract. 32 (1S) (2017) 30S–47S.
[10] A. Szlas, J.M. Kurek, Z. Krejpcio, The potential of L-arginine in prevention and treatment of disturbed carbohydrate and lipid metabolism-A review, Nutrients 14 (5) (2022).
[11] D. Tomé, Amino acid metabolism and signalling pathways: potential targets in the control of infection and immunity, Nutr. Diabetes 11 (1) (2021) 20.
[12] Z. Wang, N. Yang, Y. Hou, Y. Li, C. Yin, E. Yang, et al., L-Arginine-Loaded gold nanocages ameliorate myocardial ischemia/reperfusion injury by promoting nitric oxide production and maintaining mitochondrial function, Adv. Sci. (2023) e2302123.
[13] N. Zhang, M. Fan, Y. Zhao, X. Hu, Q. Zhu, X. Jiao, et al., Biomimetic and NOS-responsive nanomotor deeply delivery a combination of MSC-EV and mitochondrial ROS scavenger and promote heart repair and regeneration, Adv. Sci. 10 (21) (2023) e2301440.
[14] J. Jia, D.J. Richards, S. Pollard, Y. Tan, J. Rodriguez, R.P. Visconti, et al., Engineering alginate as bioink for bioprinting, Acta Biomater. 10 (10) (2014) 4323–4331.
[15] X. Wang, Y. Lei, K. Jiang, C. Yan, J. Shen, W. Zhao, et al., Mito-battery: micro-nanohydrogel microspheres for targeted regulation of cellular mitochondrial respiratory chain, Nano Today 49 (2023) 101820.
[16] Q. Chen, J. Wang, Q. Xia, L. Wu, F. Chen, L. Li, et al., Treatment outcomes of injectable thermosensitive hydrogel containing bevacizumab in intervertebral disc degeneration, Front. Bioeng. Biotechnol. 10 (2022) 976706.
[17] K. Masuda, Y. Aota, C. Muehleman, Y. Imai, M. Okuma, E.J. Thonar, et al., A novel rabbit model of mild, reproducible disc degeneration by an anulus needle puncture: correlation between the degree of disc injury and radiological and histological appearances of disc degeneration, Spine 30 (1) (2005) 5–14.
[18] S. Yuan, F. Shen, J. Bai, C.K. Chua, J. Wei, K. Zhou, 3D soft auxetic lattice structures fabricated by selective laser sintering: TPU powder evaluation and process optimization, Mater. Des. 120 (2017) 317–327.
[19] Y. Jiang, K. Shi, L. Zhou, M. He, C. Zhu, J. Wang, et al., 3D-printed auxetic-structured intervertebral disc implant for potential treatment of lumbar herniated disc, Bioact. Mater. 20 (2023) 528–538.
[20] Y. Jiang, Y. Yang, X. Zheng, Y. Yi, X. Chen, Y. Li, et al., Multifunctional load-bearing hybrid hydrogel with combined drug release and photothermal conversion functions, NPG Asia Mater. 12 (1) (2020) 18.
[21] U. Sreevidya, V. Shalini, S. Kavirajan, K.R. Maiyelvaganan, M. Prakash, K. Kamala Bharathi, et al., Investigation of non-covalent interactions in Polypyrrole/Polyaniline/Carbon black ternary complex for enhanced thermoelectric properties via interfacial carrier scattering and π-π stacking, J. Colloid Interface Sci. 630 (2023) 46–60.
[22] Y. Jiang, J. Wang, R. Wu, L. Qi, L. Huang, J. Wang, et al., Bioinspired construction of annulus fibrosus implants with a negative Poisson's ratio for intervertebral disc repair and restraining disc herniation, Bioconjugate Chem. (2023). Published online.
[23] M. Du, M. He, C. Zhu, Z. Liu, Y. Jiang, Y. Zhuang, et al., Endowing conductive polyetheretherketone/graphene nanocomposite with bioactive and antibacterial coating through electrophoresis, Macromol. Mater. Eng. (2021) 2100646.
[24] Z. Zhao, P. Zhang, W. Li, D. Wang, C. Ke, Y. Liu, et al., Pegylated recombinant human arginase 1 induces autophagy and apoptosis via the ROS-activated AKT/mTOR pathway in bladder cancer cells, Oxid. Med. Cell. Longev. 2021 (2021) 5510663.
[25] Q. Hou, Y. Dong, J. Huang, C. Liao, J. Lei, Y. Wang, et al., Exogenous L-arginine increases intestinal stem cell function through CD90+ stromal cells producing mTORC1-induced Wnt2b, Commun. Biol. 3 (1) (2020) 611.
[26] X.H. Lowman, E.A. Hanse, Y. Yang, M.B. Ishak Gabra, T.Q. Tran, H. Li, et al., p53 promotes cancer cell adaptation to glutamine deprivation by upregulating Slc7a3 to increase arginine uptake, Cell Rep. 26 (11) (2019), 3051-60.e4.
[27] L. Du, Q. Yang, J. Zhang, M. Zhu, X. Ma, Y. Zhang, et al., Engineering a biomimetic integrated scaffold for intervertebral disc replacement, Mater. Sci. Eng. C 96 (2019) 522–529.
[28] J. Xu, Y. Liu, S.H. Hsu, Hydrogels based on Schiff base linkages for biomedical applications, Molecules 24 (16) (2019).
[29] Y. Wang, Y. Wu, L. Long, L. Yang, D. Fu, C. Hu, et al., Inflammation-responsive drug-loaded hydrogels with sequential hemostasis, antibacterial, and anti-inflammatory behavior for chronically infected diabetic wound treatment, ACS Appl. Mater. Interfaces 13 (28) (2021) 33584–33599.
[30] X. Zhang, K.L. Wang, J. Hu, Y. Zhang, Y. Dai, F. Xia, Role of a high calcium ion content in extending the properties of alginate dual-crosslinked hydrogels, J. Mater. Chem. 8 (47) (2020) 25390–25401.
[31] H.K. Raut, R. Das, Z. Liu, X. Liu, S. Ramakrishna, Biocompatibility of biomaterials for tissue regeneration or replacement, Biotechnol. J. 15 (12) (2020) e2000160.
[32] H. Khatoon, S. Ahmad, A review on conducting polymer reinforced polyurethane composites, J. Ind. Eng. Chem. 53 (2017).
[33] S. Acharya, T. Kumar Bastia, B. Prasad Sahoo, Fabrication of thermoplastic polyurethane and polypyrrole conducting blends: recent advances and perspectives, Mater. Today: Proc. (2023). Published online.
[34] H. Liu, Y. Du, J.P. St-Pierre, M.S. Bergholt, H. Autefage, J. Wang, et al., Bioenergetic-active materials enhance tissue regeneration by modulating cellular metabolic state, Sci. Adv. 6 (13) (2020) eaay7608.
[35] S.M. Morris Jr., Arginine metabolism revisited, J. Nutr. 146 (12) (2016), 2579S-86S.
[36] J. Szefel, A. Danielak, W.J. Kruszewski, Metabolic pathways of L-arginine and therapeutic consequences in tumors, Adv. Med. Sci. 64 (1) (2019) 104–110.
[37] Y. Zhang, F. He, Z. Chen, Q. Su, M. Yan, Q. Zhang, et al., Melatonin modulates IL-1β-induced extracellular matrix remodeling in human nucleus pulposus cells and attenuates rat intervertebral disc degeneration and inflammation, Aging 11 (22) (2019) 10499–10512.
[38] S. Freitas-Rodríguez, A.R. Folgueras, C. López-Otín, The role of matrix metalloproteinases in aging: tissue remodeling and beyond, Biochim. Biophys. Acta Mol. Cell Res. 1864 (11, Part A) (2017) 2015–2025.
[39] C.Q. Zhao, Y.H. Zhang, S.D. Jiang, H. Li, L.S. Jiang, L.Y. Dai, ADAMTS-5 and intervertebral disc degeneration: the results of tissue immunohistochemistry and in vitro cell culture, J. Orthop. Res. : official publication of the Orthopaedic Research Society 29 (5) (2011) 718–725.
[40] N. D'Agostino, W. Li, D. Wang, High-throughput transcriptomics, Sci. Rep. 12 (1) (2022) 20313.
[41] J.S. Sousa, E. D'Imprima, J. Vonck, Mitochondrial respiratory chain complexes, Sub-cellular biochemistry 87 (2018) 167–227.
[42] D. Nolfi-Donegan, A. Braganza, S. Shiva, Mitochondrial electron transport chain: oxidative phosphorylation, oxidant production, and methods of measurement, Redox Biol. 37 (2020) 101674.
[43] P. Neupane, S. Bhuju, N. Thapa, H.K. Bhattarai, ATP synthase: structure, function and inhibition 10 (1) (2019) 1–10.
[44] I. Vercellino, L.A. Sazanov, The assembly, regulation and function of the mitochondrial respiratory chain, Nat. Rev. Mol. Cell Biol. 23 (2) (2022) 141–161.
[45] A. Perelman, C. Wachtel, M. Cohen, S. Haupt, H. Shapiro, A. Tzur, JC-1: alternative excitation wavelengths facilitate mitochondrial membrane potential cytometry, Cell Death Dis. 3 (11) (2012) e430–e.

[46] A.R. Dixon, J.P. Warren, M.P. Culbert, M. Mengoni, R.K. Wilcox, Review of in vitro mechanical testing for intervertebral disc injectable biomaterials, J. Mech. Behav. Biomed. Mater. 123 (2021) 104703.
[47] C. Neidlinger-Wilke, F. Galbusera, H. Pratsinis, E. Mavrogonatou, A. Mietsch, D. Kletsas, et al., Mechanical loading of the intervertebral disc: from the macroscopic to the cellular level, Eur. Spine J. 23 (3) (2014) 333–343.
[48] F. Fu, R. Bao, S. Yao, C. Zhou, H. Luo, Z. Zhang, et al., Aberrant spinal mechanical loading stress triggers intervertebral disc degeneration by inducing pyroptosis and nerve ingrowth, Sci. Rep. 11 (1) (2021) 772.
[49] A. Warburton, S.J. Girdler, C.M. Mikhail, A. Ahn, S.K. Cho, Biomaterials in spinal implants: a review, Neurospine 17 (1) (2020) 101–110.
[50] S. Zhang, W. Liu, S. Chen, B. Wang, P. Wang, B. Hu, et al., Extracellular matrix in intervertebral disc: basic and translational implications, Cell Tissue Res. 390 (1) (2022) 1–22.
[51] N. Bouhsina, C. Decante, J.-B. Hardel, D. Rouleau, J. Abadie, A. Hamel, et al., Comparison of MRI T1, T2, and T2* mapping with histology for assessment of intervertebral disc degeneration in an ovine model, Sci. Rep. 12 (1) (2022) 5398.
[52] T. Weichhart, Mammalian target of rapamycin: a signaling kinase for every aspect of cellular life, Methods Mol. Biol. 821 (2012) 1–14.
[53] X. Ma, M. Han, D. Li, S. Hu, K.R. Gilbreath, F.W. Bazer, et al., L-Arginine promotes protein synthesis and cell growth in brown adipocyte precursor cells via the mTOR signal pathway, Amino Acids 49 (5) (2017) 957–964.
[54] A.J. Pagán, L.J. Lee, J. Edwards-Hicks, C.B. Moens, D.M. Tobin, E.M. Busch-Nentwich, et al., mTOR-regulated mitochondrial metabolism limits mycobacterium-induced cytotoxicity, Cell 185 (20) (2022), 3720-38.e13.